



A Catalog of Molecular Clumps and Cores with Infall Signatures

Shuling Yu (于书岭)^{1,2} , Zhibo Jiang (江治波)^{1,2,3} , Yang Yang (杨旸)^{1,2} , Zhiwei Chen (陈志维)¹ , and Haoran Feng (冯浩然)^{1,2}

¹ Purple Mountain Observatory, Chinese Academy of Sciences, Nanjing 210023, China; zbjiang@pmo.ac.cn

² University of Science and Technology of China, Chinese Academy of Sciences, Hefei 230026, China

³ Center for Astronomy and Space Sciences, Three Gorges University, Yichang 443002, China

Received 2022 April 24; revised 2022 June 20; accepted 2022 June 27; published 2022 August 30

Abstract

The research of infall motion is a common means to study molecular cloud dynamics and the early process of star formation. Many works had been done in-depth research on infall. We searched the literature related to infall study of molecular cloud since 1994, summarized the infall sources identified by the authors. A total of 456 infall sources are cataloged. We classify them into high-mass and low-mass sources, in which the high-mass sources are divided into three evolutionary stages: prestellar, protostellar and H II region. We divide the sources into clumps and cores according to their sizes. The H₂ column density values range from 1.21×10^{21} to $9.75 \times 10^{24} \text{ cm}^{-2}$, with a median value of $4.17 \times 10^{22} \text{ cm}^{-2}$. The H₂ column densities of high-mass and low-mass sources are significantly separated. The median value of infall velocity for high-mass clumps is 1.12 km s^{-1} , and the infall velocities of low-mass cores are virtually all less than 0.5 km s^{-1} . There is no obvious difference between different stages of evolution. The mass infall rates of low-mass cores are between 10^{-7} and $10^{-4} M_{\odot} \text{yr}^{-1}$, and those of high-mass clumps are between 10^{-4} and $10^{-1} M_{\odot} \text{yr}^{-1}$ with only one exception. We do not find that the mass infall rates vary with evolutionary stages.

Key words: stars: formation – ISM: molecules – ISM: kinematics and dynamics – radio lines: ISM

1. Introduction

Infall motion is the initial stage of star formation. Although stars with different masses may have different formation mechanisms (e.g., Cesaroni et al. 2007; Zinnecker & Yorke 2007; Beltrán & de Wit 2016; Klassen et al. 2016), they all start from the collapse and infall of molecular cloud cores. Low-mass stars are believed to formed through inside-out gravitational collapse of dense molecular cores (Shu 1987), in which gravity overcomes thermal and nonthermal (mainly magnetic and turbulent) pressure (Zhou et al. 1993, 1994). For high-mass stars ($\geq 8 M_{\odot}$), the formation mechanism is still controversial because of the poverty of samples and the difficulty of observation due to the larger distance of star-forming region, stronger interaction with surrounding molecular clouds, and shorter star-forming timescale. There are two dominant models, one is core accretion (McKee & Tan 2002, 2003; Yorke & Sonnhalter 2002), which assumes that massive stars form as their population of low-mass stars in isolation, but that the accretion rate is a few orders of magnitude higher than low-mass stars. Another model is called competitive accretion (Bonnell & Bate 2002; Bonnell et al. 2004). This model claims that massive stars form in the dense part of molecular clumps (size $\leq 1 \text{ pc}$ and mass $\geq 200 M_{\odot}$, Beuther et al. 2005; Tan et al. 2014). They compete to accrete materials with other protostars, and the accretion continues

until the accretion condition is not satisfied. Some recent observations (e.g., Liu et al. 2013; Peretto et al. 2013; Contreras et al. 2018) support this model. In any case, infall motion is the key to initiating the formation of massive stars and maintaining accretion flows to increase mass continually during subsequent phases of evolution in these two models.

The method of finding infall samples is to identify them through special line profile. One of the significant features of infall motion is called “the spectral line asymmetry” (e.g., Zhou 1992; Mardones et al. 1997; Evans 1999; Lee et al. 1999; Wu & Evans 2003; Churchwell et al. 2010), i.e., it shows double peaks profile where the blue peak is stronger than the red one on an optically thick line, while the optically thin line has only a single peak between the double peaks of the optically thick line. The commonly used optically thick lines are CO(1–0), HCO⁺(1–0), HCO⁺(4–3), HCN(1–0), CS(2–1), H₂CO(2–1), etc. Their isotopic molecular lines, C¹⁸O(1–0), H¹³CO⁺(1–0), H¹³CO⁺(4–3), H¹³CO⁺(3–2), H¹³CN(1–0), are generally used as optically thin line to trace the system velocity. In addition, N₂H⁺(1–0) is generally optically thin, and can characterize the dense inner region of a core and well estimate the system velocity (Mardones et al. 1997; Lee et al. 1999), so it is particularly suitable for studying the structure and kinematics of star-forming cores and has been used to detect infall in IRDCs (infrared dark clouds), starless cores and protostar cores (e.g., Lee et al. 2001; Fuller et al. 2005;

Keto et al. 2015; Keown et al. 2016; Storm et al. 2016; Kim et al. 2021).

At present, there are good constraints on the formation of low-mass stars, and the corresponding evidence of infall motion has been found in the early stage until class I phase (e.g., Mardones et al. 1997; Gregersen 2000; Lee et al. 2001; Lee & Myers 2011; Padoan & Haugbølle 2014; Keown et al. 2016; Kim et al. 2021). In contrast, due to the controversy on the formation mechanism, the infall observation and research of high-mass young stellar objects (YSOs) has become more popular in recent years (e.g., Sridharan et al. 2002; Fuller et al. 2005; Klaassen & Wilson 2008; Sun & Gao 2009; Liu et al. 2011, 2013, 2020; Reiter et al. 2011; Klaassen et al. 2012; Qiu et al. 2012; He et al. 2016; Qin et al. 2016; Cunningham et al. 2018; Saral et al. 2018; Tang et al. 2019; Yang et al. 2020b; Yue et al. 2021). Rygl et al. (2013) found that the formation are closely related to the “clump-to-cloud” column density ratio. They did not find YSOs in clumps with molecular hydrogen column density less than $4 \times 10^{22} \text{ cm}^{-2}$; this ratio greater than 2 is the first sign of the beginning of star formation, and infall signature can be widely observed at this time; when the ratio greater than 3, the infall motions stop in most clumps. He et al. (2015, 2016) analyzed 732 high-mass clumps, and concluded that the detection rate of infall sources decreases gradually from prestellar to protostar and then to H II region phase; the mass of the clumps increases with these evolutionary stages whether the infall is detected or not. However, Klaassen et al. (2012) came to an abnormal situation that the detection rate of infall candidates increased significantly from protostar to hypercompact H II region phase. He thought this may be related to the beam dilution caused by smaller infall area of younger sources. Yue et al. (2021) observed 30 high-mass clumps associated with bright infrared sources, and found that the clumps with higher mass and luminosity tend to have larger mass infall rates. Large sample survey and high resolution observation of interferometric array have become the future trend of infall study.

On the basis of observation and theoretical study, the process of massive star formation is proposed by a number of researchers. Saral et al. (2018) used the classification method summarized by Motte et al. (2018): (1) starless core (Lee et al. 2001; Sohn et al. 2007; Lee & Myers 2011; Schnee et al. 2013), the gravitationally bound prestellar core or IRDC (Contreras et al. 2018); (2) hot molecular core (HMC) or protostar (Mardones et al. 1997; Fuller et al. 2005; Wu et al. 2005; Keown et al. 2016); (3) HII region (He et al. 2016). An additional stage is defined by Guzmán et al. (2015). At this stage, the expansion of the ionized gas finally destroys the molecular envelope, forming the characteristic of an extended classical H II region and a photodissociation region (PDR). Because H II still exists in this stage, but it is merely more extended, so we incorporate this stage into the stage 3. Therefore, this paper adopts the classification by Motte et al. (2018), which is divided into three main stages: prestellar, protostellar, H II region.

For simplicity, we define an infall source as a source with infall signature in this paper. There is no complete statistical work on infall sources before. Therefore we make a comprehensive search of infall study in the literature, aggregate the infall sources into a catalog, and make some statistical analysis on the physical properties.

2. The Data

2.1. Tracers

Table 1 lists the optically thick and thin lines used to identify the infall signatures collected in this paper. The frequencies and upper level of energies (E_u) in the catalog are obtained from the Splatatalogue Database.⁴ The critical density (n_{crit}) of each molecular transition is calculated by $n_{\text{crit}} = A_{ul}/\gamma_{ul}$, where A_{ul} is the Einstein A-coefficient and γ_{ul} is the collision rate coefficient for collisions with H₂ at a certain temperature. The Leiden Atomic and Molecular Database⁵ (LAMDA, Schöier et al. 2005) provides A_{ul} and γ_{ul} at different temperatures. We adopt those which are nearest E_u .

Different spectral lines can trace different properties. HCO⁺ is an abundant molecule, with particularly enhanced abundances around higher fractional ionized regions (Vasyunina et al. 2011). HCN is a good tracer of infall motion in the low-mass star-forming region. However, it may become unreliable because of a higher level of turbulence (Redman et al. 2008) and outflow signatures (Zhang et al. 2007) for the high-mass cores (Vasyunina et al. 2011). HNC is also a commonly used infall tracer. The abundance ratio HCN/HNC strongly depends on the temperature, it decreases from decades near the warm core to ~ 1 on the colder edges (Sarrasin et al. 2010).

Table 2 lists the number of sources observed by each spectral line. The upper part is the optically thick line. About 77% of the infall sources are identified with HCO⁺ (1-0), HNC (1-0) is the second most (28%). This may be because HCO⁺ (1-0) and HNC (1-0) have moderate critical density, which are high enough to trace the dense part closer to the core, and are not as high as CS (2-1), which makes it difficult to achieve such environmental conditions. In addition, the frequencies of HCO⁺(1-0) and HNC (1-0) fall in one of the best windows of atmospheric transparency, allowing them to be easily observed. Smith et al. (2013) modeled the emission produced by the hydrodynamic simulation of collapsing clouds in massive star-forming regions without outflows, and concluded that HCO⁺ (1-0) is better performed to trace collapse than HCO⁺ (4-3). Some infall studies (e.g., Fuller et al. 2005; Vasyunina et al. 2011; Rygl et al. 2013; Cunningham et al. 2018; Yuan et al. 2018; Zhang et al. 2018) that simultaneously observe multiple optically thick lines seem to support HCO⁺ (1-0) as a more effective tracer. But note that this may not be

⁴ <https://splatalogue.online>

⁵ <https://home.strw.leidenuniv.nl/~moldata/>

Table 1
Tracers Used in the Literature

Serial Number	Spectral line	Transition	Rest Frequency ^a (GHz)	E_u^a (K)	n_{crit}^b (cm ⁻³)
Optically Thick Lines					
1	HCO ⁺	$J = 1 - 0$	89.188,526	4.28	1.6×10^5
2	HCO ⁺	$J = 3 - 2$	267.557,633	25.68	3.7×10^6
3	HCO ⁺	$J = 4 - 3$	356.734,242	42.80	9.3×10^6
4	CO	$J = 2 - 1$	230.538,000	16.60	1.1×10^4
5	CO	$J = 3 - 2$	345.795,990	33.19	3.7×10^4
6	CO	$J = 4 - 3$	461.040,768	55.32	9.1×10^4
7	HNC	$J = 1 - 0$	90.663,564	4.35	2.8×10^5
8	HNC	$J = 4 - 3$	362.630,304	43.51	2.0×10^7
9	HCN	$J = 1 - 0$	88.631,602	4.25	1.0×10^6
10	HCN	$J = 3 - 2$	265.886,434	25.52	6.8×10^7
11	CS	$J = 2 - 1$	97.980,953	7.05	3.3×10^7
12	H ₂ CO	$J_{kk'} = 2_{12} - 1_{11}$	140.839 518	21.9	7.7×10^5
13	CN	$N = 2 - 1, J = 3/2 - 1/2, F = 5/2 - 3/2$	226.659,558	16.31	1.3×10^7
14	C ¹⁸ O	$J = 2 - 1$	219.560,358	15.81	9.3×10^3
15	¹³ CO	$J = 3 - 2$	330.587,965	31.73	3.3×10^4
16	CH ₃ CN	$J = 19 - 18 K = 3$	349.393,297	232.0	1.6×10^7
Optically Thin Lines					
1	N ₂ H ⁺	$J = 1 - 0$	93.173,404	4.47	1.4×10^5
2	H ¹³ CO ⁺	$J = 1 - 0$	86.754,288	4.16	1.5×10^5
3	H ¹³ CO ⁺	$J = 3 - 2$	260.255,339	24.98	3.2×10^6
4	C ¹⁸ O	$J = 1 - 0$	109.782,176	5.27	1.9×10^3
5	C ¹⁸ O	$J = 2 - 1$	219.560,358	15.81	9.3×10^3
6	C ¹⁷ O	$J = 3 - 2$	337.061,130	32.35	3.5×10^4

Note. *a*: The rest frequency of the line and upper level of energy values are obtained from the splatalogue database. *b*: the critical density are derived from the formula $n_{\text{crit}} = A_{ul}/\gamma_{ul}$.

always true, for example, Tsamis et al. (2008) show that HCO⁺ (4-3) may be a better tracer to detect the asymmetry than HCO⁺ (1-0) at earlier times.

The observation of optically thin lines is also particularly crucial. Multiple velocity component, for example, the colliding fragments of two clouds, could produce the double-peaked blue profile, but they would also produce a double-peaked profile in the optically thin line (Evans 1999). In order to eliminate this situation, the optically thin line must have only a single peak between the two peaks of the optically thick line. The lower part of Table 2 lists the optically thin lines used in the articles. Different line widths of optically thin lines will affect the estimation of skewness parameters, see Section 3.4.

2.2. The Catalog

Up to May 2021, a total of 456 infall candidates have been identified, including 352 (77%) sources being associated with high-mass star-forming regions, and 55 (12%) with low mass, the remaining 49 (11%) being uncertain. The low-mass sources are fewer, probably due to the more attention has been paid to high-mass sources in recent years, meanwhile the weakness of infall characteristics of low-mass sources. Of these sources,

eight are observed by interferometric array, accounting for a small proportion and will not be discussed separately, the others are observed by single-dish telescope.

We divide the sources into clumps and cores as their properties may be different in infall motion. He et al. (2015) counted the sources and found that more than 96.6 per cent of clumps have masses higher than $100 M_{\odot}$. Saral et al. (2018) thought that the dense cores have sizes <0.1 pc and masses $<100 M_{\odot}$. This paper adopts such a grouping criterion: when the radius of a source lower than 0.1pc (main criteria) and mass lower than $100 M_{\odot}$, we believe this source is a core, otherwise, it is classified as a clump. For those sources whose radius data are not given in the literature, we use the calculated distance and the spatial resolution of the telescope to estimate the radius. Of all the 456 sources, 396 (87%) are clumps and 60 (13%) are cores. For 352 high-mass sources, 343 (97%) are clumps, and for 54 low-mass sources, 46 (85%) are cores. That is, vast majority of the high-mass sources are clumps, and most of the low-mass sources are cores. Therefore, we ignore the influence of these few parts and only discuss the statistical properties of high-mass clumps and low-mass cores. The difference of statistical results is less than 5% when the samples are roughly

Table 2
The Number of Sources Observed by Tracers

Serial Number	Spectral Line	Number of Sources	Reference
Optically Thick Lines			
1	HCO ⁺ (1–0)	350	3, 5, 10, 12, 13, 14, 15, 16, 17, 18, 19, 20, 21, 27, 28
2	HCO ⁺ (3–2)	30	2, 6, 7, 9, 19, 20, 22, 23, 24, 25, 27, 30, 31
3	HCO ⁺ (4–3)	18	13, 22, 23, 27, 30
4	CO(2–1)	24	13
5	CO(3–2)	8	13
6	CO(4–3)	18	1, 29
7	HNC(1–0)	129	12, 28
8	HNC(4–3)	1	22, 23, 30
9	HCN(1–0)	48	3, 26, 31
10	HCN(3–2)	8	5, 9, 11, 14, 15, 19, 20
11	CS(2–1)	24	6, 19, 20, 21, 22, 23, 24, 30, 31
12	H ₂ CO(2 ₁₂ –1 ₁₁)	26	22, 23, 27, 30
13	CN(<i>N</i> =2–1, <i>J</i> =3/2 – 1/2, <i>F</i> =5/2 – 3/2)	3	5, 8, 10, 14, 16, 20
14	C ¹⁸ O(2–1)	1	7
15	¹³ CO(3–2)	1	10, 14, 16, 20
16	CH ₃ CN(<i>J</i> =19 – 18, <i>K</i> =3)	1	4
Optically Thin Lines			
1	N ₂ H ⁺ (1–0)	304	6, 12, 22, 26, 27, 28
2	H ¹³ CO ⁺ (1–0)	56	13, 14
3	H ¹³ CO ⁺ (3–2)	32	19, 25, 27
4	C ¹⁸ O(1–0)	77	3, 6, 20
5	C ¹⁸ O(2–1)	33	13
6	C ¹⁷ O(3–2)	18	1

References are: 1: Yue et al. (2021), 2: Contreras et al. (2018), 3: Yang et al. (2020a), 4: Liu et al. (2020), 5: Liu et al. (2013), 6: Lee et al. (2001), 7: Tang et al. (2019), 8: Qiu et al. (2012), 9: Qin et al. (2016), 10: Wu et al. (2009), 11: Liu et al. (2011), 12: He et al. (2015), He2016, 13: Rygl et al. (2013), 14: Klaassen et al. (2012), 15: Klaassen & Wilson (2007), 16: Klaassen & Wilson (2008), 17: Sridharan et al. (2002), 18: Kurtz et al. (1994), 19: Reiter et al. (2011), 20: Sun & Gao (2009), 21: Shirley et al. (2003), 22: Mardones et al. (1997), 23: Su et al. (2019), 24: Lee & Myers (2011), 25: Gregeresen et al. (1997), Gregeresen2000, 26: Kim et al. (2021), 27: Fuller et al. (2005), 28: Saral et al. (2018), 29: Faúndez et al. (2004), 30: Di Francesco et al. (2001), 31: Keown et al. (2016).

divided into high-mass and low-mass sources compared with which are grouped into clumps and cores.

Table 3 lists the first ten sources of the infall catalog and their physical parameters. The complete catalog is in table A.1 of the Appendix. All the parameters are fetched from the literature, except the distance.

3. Statistics and Distribution

3.1. Spatial Distribution

Figure 1 shows the galactic distribution of all infall sources overlaid on the imaginary face-on image of the Milky Way, which is adopted from “Xing-Wu Zheng & Mark Reid BeSSeL/NJU/CFA⁶”, and which is believed to be currently the most scientifically accurate visualization of the Milky Way. The blue circle indicates the location of the Sun, with a distance 8.15 kpc to the Galactic center (Reid et al. 2019). The red pentagram represents the location of the infall sources. The scale of the image is indicated in the lower left corner of the figure. We found that most of the sources (about 90%) are

located within 5 kpc of the Sun. This may be caused by the observation effect. Moreover, The numbers of infall sources inside and outside the solar circle are 390 and 66, respectively. Although the observations to date are far from complete, the present evidence shows that the star formation activity inside the solar circle is more intense than the outside (Djordjevic et al. 2019), which needs further investigation in the future. Some infall sources are distributed on the spurs between the Local and Sagittarius arms (Xu et al. 2016) and between the Sagittarius and Scutum arms.

3.2. Excitation Temperature

The excitation temperature T_{ex} is usually estimated using the standard radiation transfer equation and assuming local thermodynamic equilibrium (LTE).

Of all the sources, there are 109 that have valid T_{ex} values, all of them are fetched from the literature. we do not differentiate these sources by high mass or low mass because of the relatively small number. The median and mean value of T_{ex} are 12.3 K and 13.4 K respectively. Figure 2(a) shows the distribution of T_{ex} of all, and (b) shows the distribution of T_{ex}

⁶ <https://astronomy.nju.edu.cn/xtzl/EN/>

Table 3
The Catalog of all Collected Infall Sources

No.	R.A.	Decl.	Alias	Dist.	V_{LSR}	$N(\text{H}_2)$	$n(\text{H}_2)$	Mass	Lines	δv	V_{in}	\dot{M}_{in}	Type	Stage	Maser	Outflow	Reference
(1)	(J2000)	(J2000)	(4)	(kpc)	(km s $^{-1}$)	(cm $^{-2}$)	(cm $^{-3}$)	(M_{\odot})	(10)	(11)	(km s $^{-1}$)	(M_{\odot} yr $^{-1}$)	(14)	(15)	(16)	(17)	(18)
	(2)	(3)		(5)	(6)	(7)	(8)	(9)			(12)	(13)					
1	00:35:40.1	+66:14:23	G121.34 + 3.42	0.18	-5.3	9.8E+21			1, 9	-0.47							3
2	00:36:47.5	+63:29:01	G121.30 + 0.66	0.9	-17.6				2	-0.54			high		123	Y	19
3	00:36:53.6	+63:28:03	G121.31 + 0.64	1.1	-17.3	1.7E+22			1,9	-0.63	0.29	1.6E-3		2			3
4	00:52:25.1	+56:33:54	G123.07-6.31	2.2	-30.4				1, 2,10	-0.20			high	3	123	Y	19,20
5	02:19:51.8	+61:03:26	G133.42 + 0.00	0.9	-15.2	4.8E+21			9	-0.59				2			3
6	02:27:03.8	+61:52:25	W3(OH)	2.4	-48.0		6.0E+6		1,10	-0.23	0.06	3.0E-4	high	3	1234	Y	14,15,19,20
[†] 7 [*]	02:27:04.7	+61:52:26	W3(H ₂ O)	2.0	-47.8	2.6E+24	1.0E+8	2.6E+1	2,10	-0.65	2.70	2.3E-3	high	2	1234	Y	9
[†] 8	02:53:12.2	+68:55:52	LDN 1355	0.3	-3.8	1.4E+21	9.1E+3		11	-0.42	0.12	8.4E-6	low	1			6,24
[†] 9	03:26:37.0	+30:15:26	IRAS03235 + 3004	0.35	4.9				2	-0.66			low	2	3		25
[†] 10	03:28:32.5	+31:11:05	J03283258 + 3111040	0.3	7.2				9	-0.45	0.17	6.5E-6	low	2			26

The columns are as follows:

- (1): internal serial number. Sources that are observed by interferometric array are signed with * in the upper right. The symbol [†] in the upper left indicates that the source is considered as a core, and the rest are clumps;
(2), (3): the R.A. and decl. (J2000);
(4): the alias names of sources based on Galactic Coordinates;
(5): the distance of each source, which are calculated by the parallax-based distance estimator⁷ (Reid et al. 2016, 2019). It used the Bayesian approach to assign sources to spiral arms based on their (l , b , v) coordinates with respect to arm signatures seen in CO and H I surveys. The estimator gives two most likely values of distance from the full distance probability density function, and use the parameter P to control the prior probability of obtaining a near/far distance. We also calculated the scale height of each source by using the maximum likelihood distance. We found that for some sources, the scale height will be much larger than that of molecular gas disk, that is, ~ 280 pc (Su et al. 2021). In such cases the near distance is adopted, although the probability of the far distance given by the estimator is greater;
(6): the velocity corresponding to the peak position of the optically thin line. Some sources have been observed by more than one groups, they may give different parameters in such cases, we adopt the most recent one. This applies to columns 6–13, except column 10;
(7), (8): the column density and number density (assumed to be spherical) of H₂;
(9): mass;
(10): optically thick lines that show blue asymmetry. The number is the same as that in Table 1, and the bold font indicate the one being used to calculate δv ;
(11): measure of asymmetry of the spectral profile. If multiple optically thick lines are used to identify infall motion, and multiple values are obtained accordingly, then we choose the one considered to be most effective in the paper, see Section 3.4;
(12): infall velocity;
(13): mass infall rate;
(14): the mass type of the source, *high* and *low* denote high-mass and low-mass, respectively;
(15): evolutionary stage. The number 1, 2, 3 refer to stages of prestellar, protostellar and H II region for high-mass sources and 1, 2 for low-mass ones. Sources labeled as CH II (compact H II) or HCH II (hyper-compact H II) or UCH II (ultra-compact H II) in the literature are all merged into category 3 in this work;
(16): the maser associated with these sources in the range of 1'. The number 1, 2, 3, 4 represent the maser of CH₃OH-I, CH₃OH-II, H₂O, OH, respectively;
(17): the sources associated with outflow provided in some literature (Wu et al. 2004; Maud et al. 2015; Li et al. 2019; Zhang et al. 2020) within 2';
(18): references. The number is the same as listed in Table 2. The angular resolution and sensitivity of adopted observations are listed below according to the sequence of references. 1: 13'', 0.19 K at 0.27 km s $^{-1}$ for CO (4-3) and 0.14 K at 0.27 km s $^{-1}$ for C¹⁷O (3-2), 2: 1''2, 0.14 K at 0.08 km s $^{-1}$, 3: 62'', 0.1 K at 0.2 km s $^{-1}$, 4: 0''14, 5: 18''3, 0.15 K for HCN (3-2), 6: 52'', 7: 3''74 \times 3''04 (-86°) for C¹⁸O (2-1), 0''86 \times 0''86 (85°) for HCO⁺(3-2), 8: 1''4 \times 1''3 (57°) for CN ($N = 2-1$), 9: 2''3 \times 2''1 (-60°), 11: 1''63 \times 1''28 ($-81^{\circ}4$), 12: 19''2, 13: 28'', 0.10 K at 0.08 km s $^{-1}$ for HCO⁺(1-0), and 11'', 1.3 K at 1.5 km s $^{-1}$ for CO (2-1), 14: 15'', 0.1 K at 0.42 km s $^{-1}$ (356 GHz) and 0.07 K at 0.82 km s $^{-1}$ (347 GHz), 15: 14'', 0.13 K at 0.53 km s $^{-1}$, 16: 14'', 0.13 K at 0.42 km s $^{-1}$, 19: 18'', 20: 55'', ~ 0.07 K, 21: 24''5, 22: 28'', 23: 16''55, 24: 52'', 25: 26'', 26: 32'', ~ 0.4 K at 0.11 km s $^{-1}$, 27: 29'' (IRAM), 14'' (JCMT), 0.08 K for HCO⁺(4-3) and 0.07 K for HCO⁺(1-0), 28: 38'', 29: 24'', 30: $\sim 2''$, 31: 9''4, 0.02 K at 0.044 km s $^{-1}$.

⁷ <http://bessel.vlbi-astrometry.org/node/378>

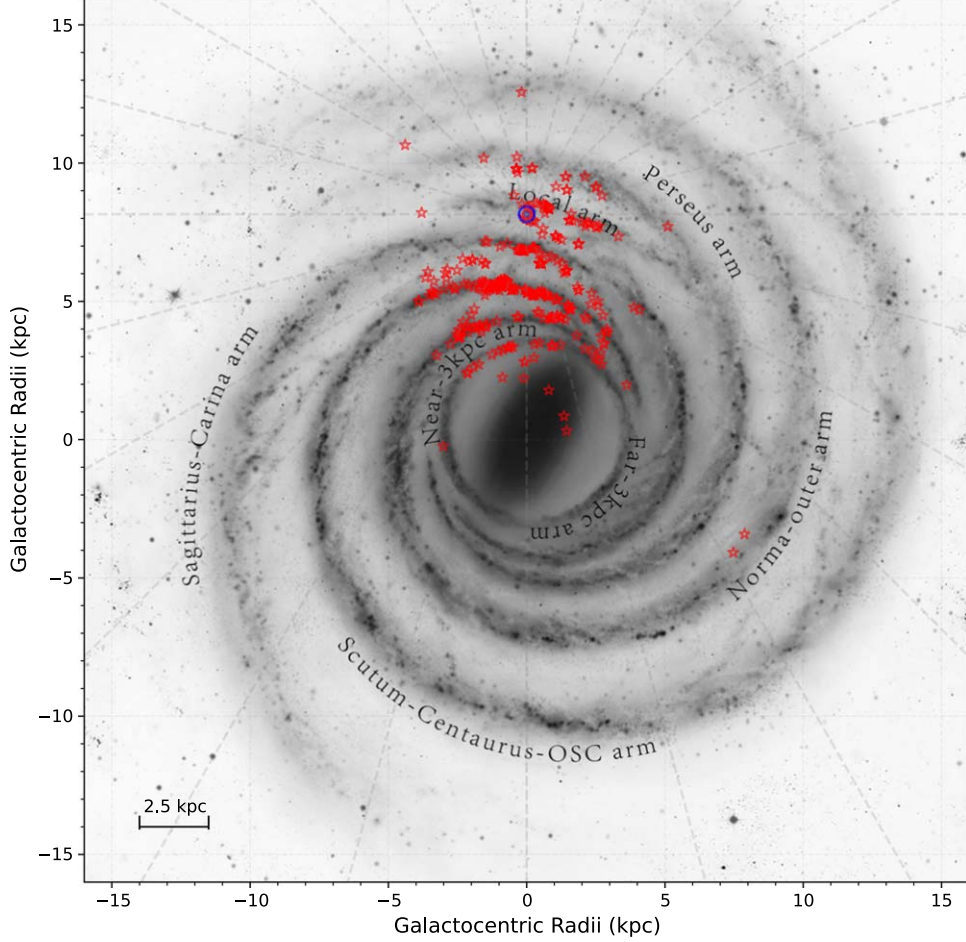


Figure 1. Galactic distribution of the infall sources. The blue circle indicates the location of the Sun. The red pentagram represents the location of the infall sources. The background is the imaginary face-on image of the Milky Way (created: “Xing-Wu Zheng & Mark Reid BeSSeL/NJU/CFA”).

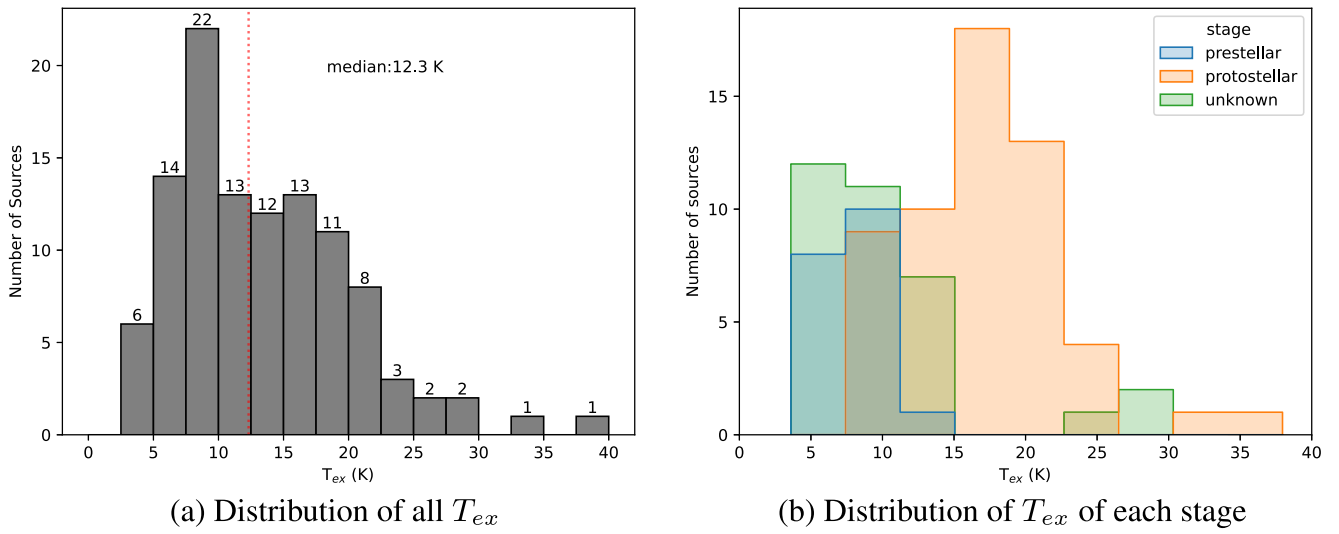
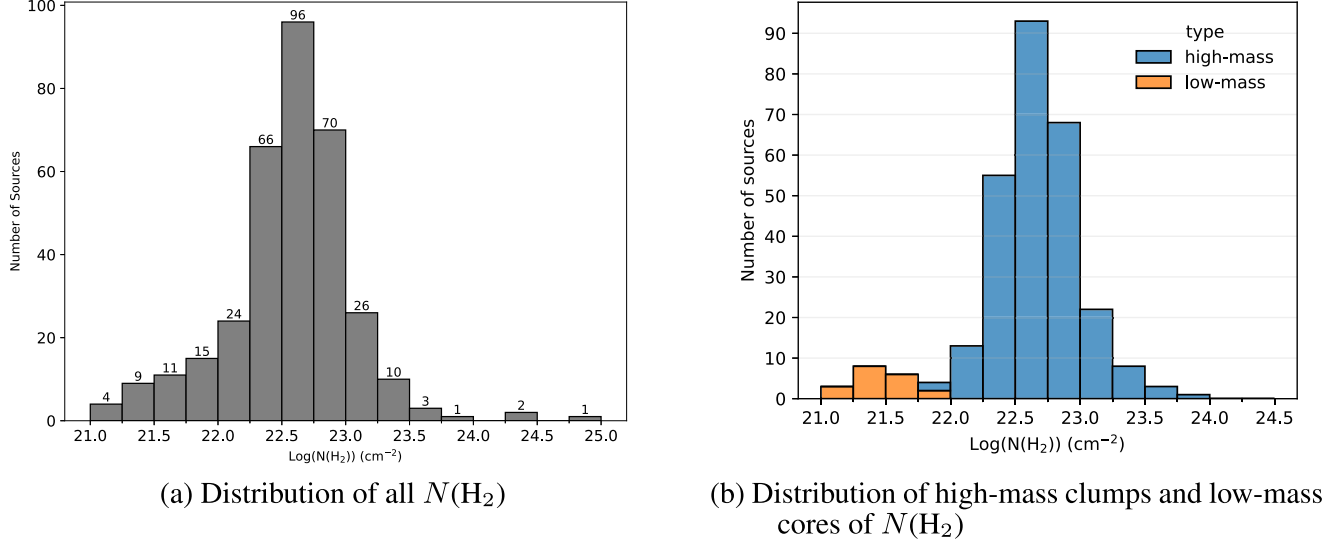
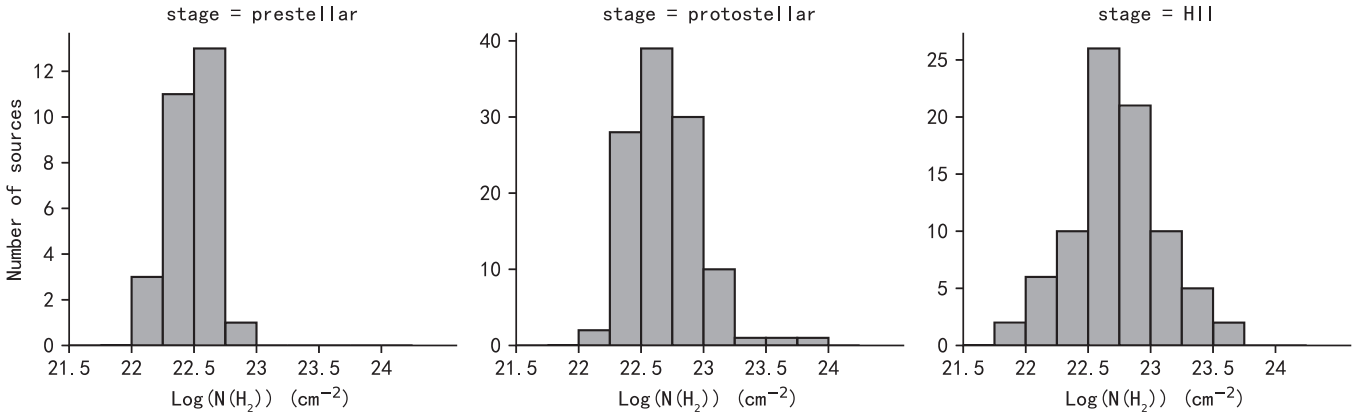


Figure 2. Distribution of T_{ex}

Figure 3. Distribution of H_2 column densityFigure 4. Distribution of H_2 column density for high-mass clumps at different evolutionary stages.

of each stage. It can be seen from Figure 2(b) that the excitation temperatures in the protostellar stage are significantly higher than those in the prestellar stage, and their median values are 17.1 K and 7.8 K respectively. It may be because of the fact that in the prestellar stage, it is too early to release enough gravitational energy to heat the surrounding environment. However, this trend should be interpreted with caution due to the small number of samples.

3.3. Column Density

Figure 3(a) shows the H_2 column density N_{H_2} distribution of all sources with valid values given in the literature. The column density of H_2 ranges from 1.2×10^{21} to $9.8 \times 10^{24} \text{ cm}^{-2}$, with a median value of $4.17 \times 10^{22} \text{ cm}^{-2}$. Figure 3(a) shows that N_{H_2} is not log-normally distributed. Figure 3(b) gives the

column density distributions of low-mass and high-mass sources. It can be seen that the N_{H_2} distribution of low-mass cores and high-mass clumps is significantly separated. Their median values are 2.6×10^{21} and $4.8 \times 10^{22} \text{ cm}^{-2}$, respectively. Among them, there are few samples of low-mass cores, so its distribution has little significance. For high-mass clumps, the distribution has a threshold of $10^{22} \sim 10^{24} \text{ cm}^{-2}$, which is consistent with the literature (Rygl et al. 2013; He et al. 2016). Figure 4 presents the distribution of N_{H_2} for high-mass clumps at different evolutionary stages. The median values for high-mass are 3.1×10^{22} , 4.7×10^{22} , $5.4 \times 10^{22} \text{ cm}^{-2}$ for prestellar, protostellar, H II, respectively. Taking into account that the corresponding rms are 0.18, 0.28, 0.35 in the case of logarithm, respectively, the column density of H_2 increases slightly with the evolutionary stage. Different methods for calculating column density are used in different papers, the results of

column density calculated using different molecular lines are different based on abundance ratios to hydrogen molecules.

3.4. The Skewness Parameter

As stated in the introduction, the infall motion is signified by the spectral line asymmetry of optically thick line and a single-peaked profile (Leung & Brown 1977; Zhou 1992; Mardones et al. 1997; Evans 1999; Lee et al. 1999). To demonstrate the measure of asymmetry, Mardones et al. (1997) defined a non-dimensional parameter δV

$$\delta V = \frac{V_{\text{thick}} - V_{\text{thin}}}{\Delta V_{\text{thin}}}, \quad (1)$$

where V_{thick} and V_{thin} are the velocities of the peaks of optically thick and thin lines. ΔV_{thin} is the line width (FWHM) of the optically thin line. The values δV obtained from different line pairs may be different. When $\delta V \leq -0.25$ or $\delta V \geq 0.25$, it can usually be considered that the source has a significant blue or red profile.

Different molecules may give different result in studying infall. Mardones et al. (1997) observed 47 protostars to identify infall sources with H₂CO (2₁₂-1₁₁) and CS (2-1), and found that the fraction of blue profiles decrease from Class 0 to Class I. However, Gregersen (1998) observed a larger sample which includes the Class I sources of Mardones et al. (1997), but did not find such trend using HCO⁺(3-2). Fuller et al. (2005) observed HCO⁺ $J=1-0$, $J=3-2$, $J=4-3$, and H₂CO (2₁₂-1₁₁) toward 77 850 μm continuum sources, and suggests HCO⁺(1-0) and H₂CO (2₁₂ - 1₁₁) trace infall more effectively than HCO⁺(3-2) and HCO⁺(4-3). Rygl et al. (2013) used HCO⁺(1-0), HCO⁺(4-3) and CO (3-2) to observe another sample of high infrared extinction clouds, came to a similar conclusion. Therefore, the δV values derived from HCO⁺(1-0) and H₂CO (2₁₂-1₁₁) are given with high priority.

Figure 5 shows the distribution of 429 valid δV values of all sources. Although δV s are calculated from different lines, we believe this distribution has its scientific significance since the large proportion is identified with HCO⁺(1-0). The median value of δV for all sources is -0.52. For high-mass clumps, the median value identified with HCO⁺(1-0) is -0.50. In contrast, Rygl et al. (2013) derived -0.64 with the same line. For low-mass cores, Figure 6 presents the δV distribution of different evolutionary stages. The median values at stages of prestellar and protostellar are -0.46 and -0.74, respectively. Considering the corresponding rms are 0.16 and 0.33 respectively, the blue asymmetry may have no difference with evolution of low-mass cores. Further observations are needed because of the small sample size. As Figure 7 shows, the δV of high-mass infall clumps are -0.55, -0.52, -0.47 at the stage of prestellar, protostellar and H II region respectively. The rms are 0.23, 0.29, 0.25, respectively. It seems that the blue

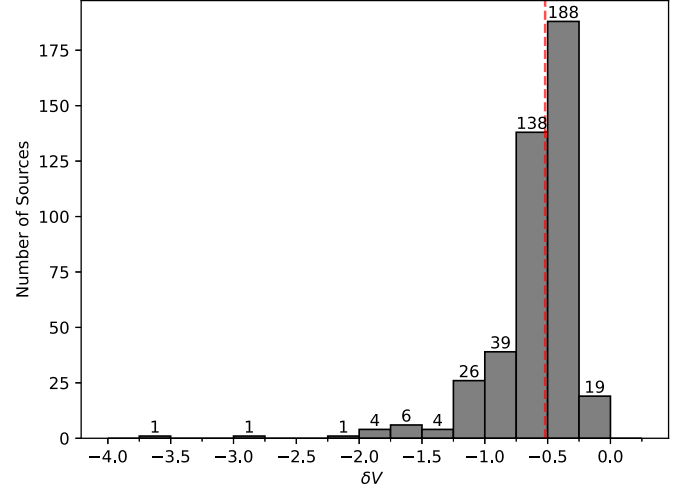


Figure 5. Distribution of δV for all sources given in the literature. The red dotted line represents the median value of δV .

asymmetry of high-mass infall clumps have the same trend as those of low-mass.

3.5. Infall Velocity

So far, there are several different approaches to estimate the infall velocity: velocity difference, “two-layer” model, “hill” model, RATRAN, etc. (i) Some works (e.g., Liu et al. 2013; He et al. 2015, 2016; Su et al. 2019) estimated roughly with $V_{\text{in}} = V_{\text{obs}} - V_{\text{sys}}$, where V_{obs} means the velocity at blue peak of the optically thick line, V_{sys} is the system velocity from Gaussian fit of the optically thin line. (ii) The “two-layer” model (Myers et al. 1996) assumes that the excitation temperature in each layer is constant. Some works (e.g., Lee et al. 2001; Qin et al. 2016; Tang et al. 2019; Yue et al. 2021) used the “two-layer” model to calculate the infall velocity with the following equation when $V_{\text{in}} \ll \sigma(2 \ln \tau_0)^{1/2}$,

$$V_{\text{in}} = \frac{\sigma^2}{V_{\text{red}} - V_{\text{blue}}} \ln \left(\frac{1 + e^{(T_{\text{blue}} - T_{\text{dip}})/T_{\text{dip}}}}{1 + e^{(T_{\text{red}} - T_{\text{dip}})/T_{\text{dip}}}} \right), \quad (2)$$

where V_{blue} and V_{red} are the velocities of the blue and red peaks of optically thick line, T_{blue} and T_{red} are the corresponding peak intensities, T_{dip} is the intensity of self-absorption dip between the two peaks, and σ is the velocity dispersion of optically thin line. (iii) The “hill” model assumes that the excitation temperature is increase inward as a linear function of optical depth (De Vries & Myers 2005). De Vries & Myers (2005) thought that the “two-layer” model underestimates the infall velocity by a factor of ~ 2 when matching the two-peak profiles while the “hill” model matches better with an rms error of 0.01 km s⁻¹. Blue-asymmetric line profiles with shoulder or redshifted peak cannot generally well fitted by the “two-layer” or “hill” model. (iv) A more complex model is RATRAN,

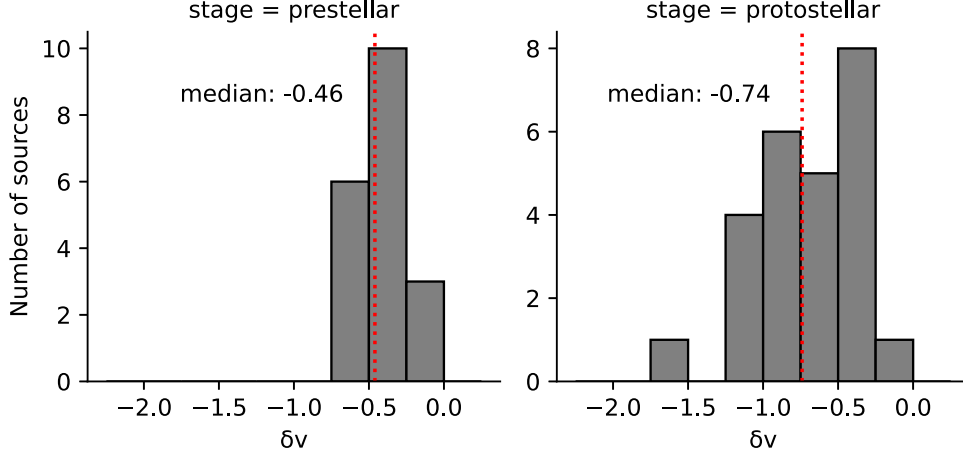


Figure 6. Distribution of δV for low-mass cores. The red dotted line represents the median value of δV for each stage.

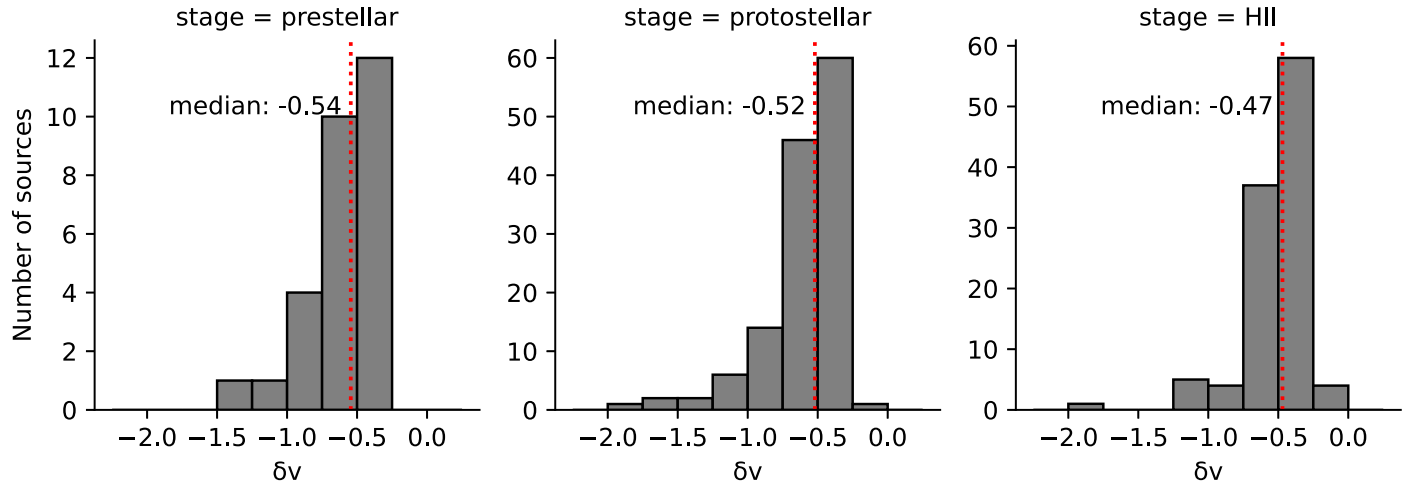


Figure 7. Distribution of δV for high-mass clumps. The red dotted line represents the median value of δV for each stage.

which uses 1D Monte Carlo radiative transfer code (Hogerheijde & Van Der Tak 2000) to construct the infall model with more input parameters, such as the radius, mass, density profile, turbulent velocity, kinetic temperature distribution, and the abundance of the molecule. This model can better constrain infall velocity than the ‘two-layer’ model (Peretto et al. 2013). The infall velocities derived by different approaches are relatively uniform and will not have a significant impact on the statistical results.

Figure 8 shows the distribution of infall velocities for 354 sources provided in the literature. We give the fitting of lognormal distribution (blue dashed line). The parameters are marked in the upper right of the figure. Kolmogorov-Smirnov (KS) test shows the P value is 0.31. The median value (red dotted line) is 0.97 km s^{-1} . The infall velocity varies with tracers and position across

each core (Keown et al. 2016). Liu et al. (2013) believes that infall velocity may be related to the stage of evolution. In order to further study this, we conduct research according to different type of mass and stages. Figure 9 shows the distribution of infall velocity to different evolutionary stages of low-mass cores. The V_{in} of almost all low-mass sources are less than 0.5 km s^{-1} . This is rather different from the result of Liu et al. (2013), which shows the typical infall velocities in low-mass star-forming regions are $\sim 0.5 \text{ km s}^{-1}$. The median values of prestellar and protostellar stage are $0.05 (\pm 0.04)$ and $0.17 (\pm 0.20) \text{ km s}^{-1}$, suggest that V_{in} may not change with evolution for low-mass cores. However, this result should be interpreted with caution and await further investigation. KS test assumes that the distribution of these two stages is consistent, and the P value is 0.013, rejecting the original hypothesis.

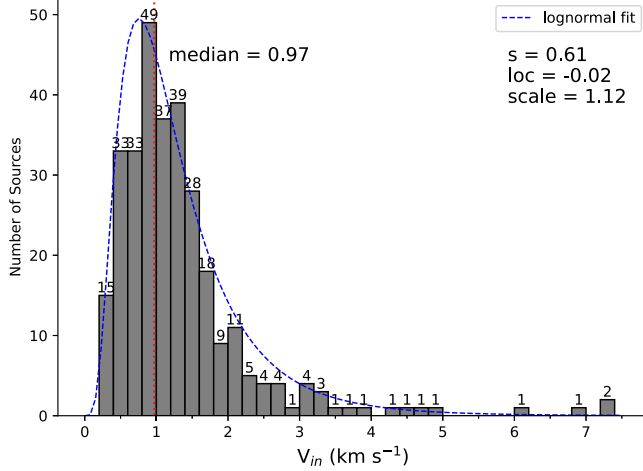


Figure 8. Distribution of infall velocity. The red dotted line indicates the median value. The blue dashed line is the fitting of lognormal.

Figure 10 shows the distribution of infall velocities for high-mass clumps at different stages. The median values of prestellar, protostellar and H II region are $1.08 (\pm 0.49)$, $1.14 (\pm 0.62)$ and $1.07 (\pm 1.11)$ km s⁻¹, respectively, implying that the infall velocities of the high-mass clumps have a similar trend to that of the low-mass cores, that is, it may not change with evolutionary stages. It can be seen from the figure that the distributions of these three stages are roughly the same. To confirm this, we performed the KS test, assuming the same distribution. The P value for the first two stages is 0.72, and for the stage of protostellar and H II is $P = 0.59$, which show that the original hypothesis is not rejected. Skewness is a metrics of the distribution and extent of statistical data, defined as $\text{skew}(X) = E\left[\left(\frac{X-\mu}{\sigma}\right)^3\right]$, which can characterize distribution asymmetry. The skewness of the three stages of the massive infall clumps are 1.10, 1.10, 2.10, respectively, which indicates that the distribution of V_{in} tends to be symmetrical at the first two evolutionary stages, while it tends to be right wing at the H II region stage.

We have also analyzed the influence of different spectral lines on the infall velocity of the sources. The lines adopted by at least 15 sources are used for the following statistics. They are: HCO⁺(1–0), CO (4–3), CS (2–1). For the cores with valid V_{in} values, only CS (2–1) meets the statistical requirement. The median value is $0.05 (\pm 0.04)$ km s⁻¹, which is basically consistent with the median value 0.07 km s⁻¹ of all low-mass cores. This result may change as the sample number of low-mass cores increases. For high-mass clumps, The median values estimated by HCO⁺(1–0) and CO (4–3) are $1.03 (\pm 0.85)$, $3.21 (\pm 1.45)$ km s⁻¹, respectively. The number of V_{in} estimated by HCO⁺(1–0) accounts for more than 90%, and is

thus close to the median value 1.06 of all the high-mass clumps. The sources using CO (4–3) to derive V_{in} are all from Yue et al. (2021).

On the other hand, Rygl et al. (2013) calculated the source (G014.63–00.57 MM1) and showed that the V_{in} derived from HCO⁺(1–0) is about twice as large as that derived from HCO⁺(4–3), but he thought the value derived from HCO⁺(1–0) was overestimated. Saral et al. (2018) used two lines (HCO⁺ and HNC) to estimate infall velocities of the same three sources, the results were similar taking into account the error. Tang et al. (2019) estimated V_{in} of one source (G192.16–3.84) with C¹⁸O (2–1) and HCO⁺(3–2), indicating that the result derived from HCO⁺(3–2) is slightly larger than C¹⁸O (2–1). It can be seen that, due to the lack of total samples, we are temporarily unable to systematically study the influence of different spectral lines on the infall velocity.

3.6. Mass Infall Rate

The mass infall rate can be estimated by

$$\dot{M}_{\text{in}} = 4\pi R^2 \mu m_{\text{H}} n_{\text{H}_2} V_{\text{in}}, \quad (3)$$

where $\mu = 2.8$ (Wang et al. 2014) is the mean molecular weight, m_{H} is the mass of the hydrogen atom, R is the radius of source (here the source is assumed to be spherical), V_{in} is the infall velocity, n_{H_2} is the mean volume density, which has a conversion relationship with the column density N_{H_2} :

$$n_{\text{H}_2} = \frac{3N_{\text{H}_2}}{R}. \quad (4)$$

Figure 11 shows the distribution of mass infall rate of the sources provided in the literature. We could see from the figure that the distribution can be divided into two parts, this separation comes from the different types of mass. Among them, we do not know the distribution of low-mass cores because of fewer samples, but for high-mass clumps, it presents an evident lognormal distribution with the P value of 0.82 of KS test. The range of mass infall rate for low-mass cores are 10^{-7} – 10^{-4} $M_{\odot}\text{yr}^{-1}$, and almost all high-mass clumps are 10^{-4} – 10^{-1} $M_{\odot}\text{yr}^{-1}$ with only one exception. This is consistent to previous work in high-mass star-forming regions range between 10^{-4} – 10^{-2} $M_{\odot}\text{yr}^{-1}$ (e.g., Wu et al. 2009; Qiu et al. 2012; Liu et al. 2013; Qin et al. 2016), which are far larger than that of low-mass sources (Beuther et al. 2005; Padoan & Haugbølle 2014; Kim et al. 2021).

Padoan & Haugbølle (2014) proposed that in most cases, the \dot{M}_{in} is initially the order of 10^{-5} $M_{\odot}\text{yr}^{-1}$, and may decay rapidly when forming low-mass stars, or maintain relatively large when forming massive stars. Yue et al. (2021) concluded that mass infall rate is independent of the evolutionary stage. Figure 12 shows the distribution of mass infall rate for sources at different evolutionary stages. The orange represents low-mass cores and the blue represents high-mass clumps. The

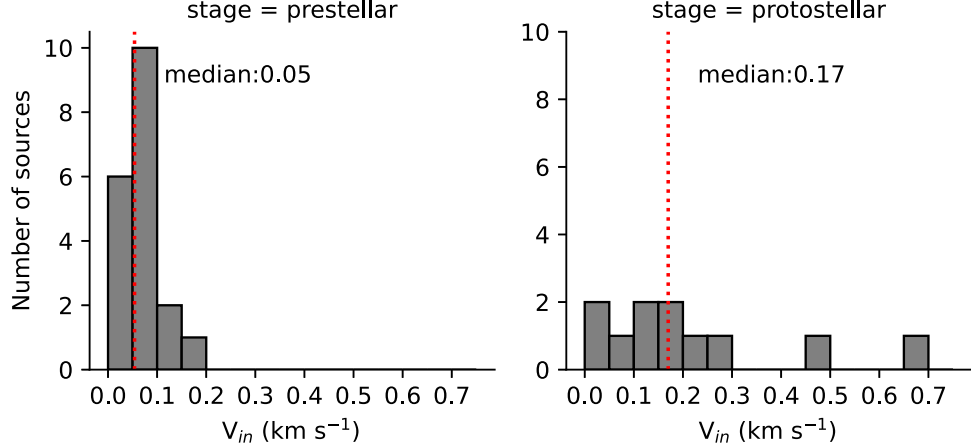


Figure 9. Distribution of infall velocity at different evolutionary stages for low-mass cores. The red dotted line represents the median value for each stage.

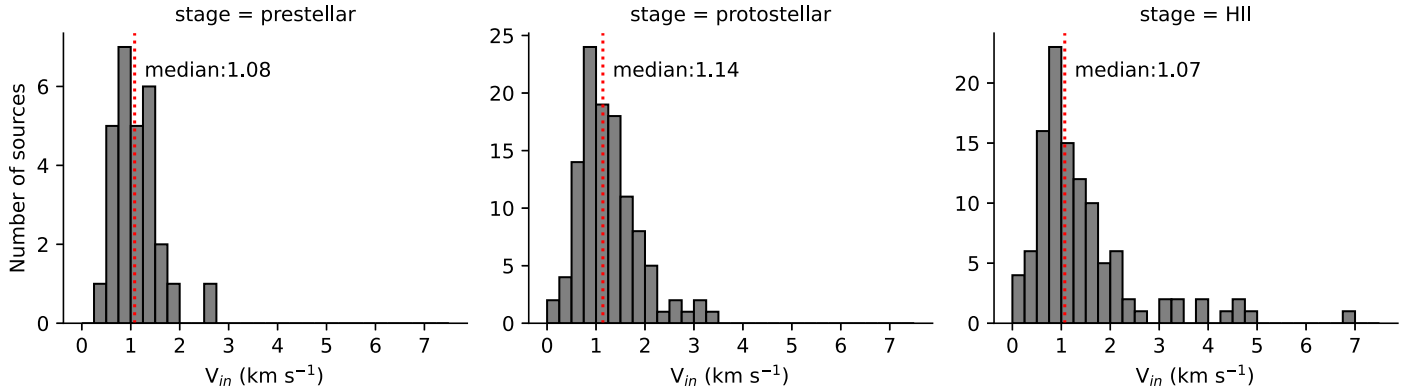


Figure 10. Distribution of infall velocity for high-mass clumps at different evolutionary stages. The red dotted line represents the median value of V_{in} for each stage.

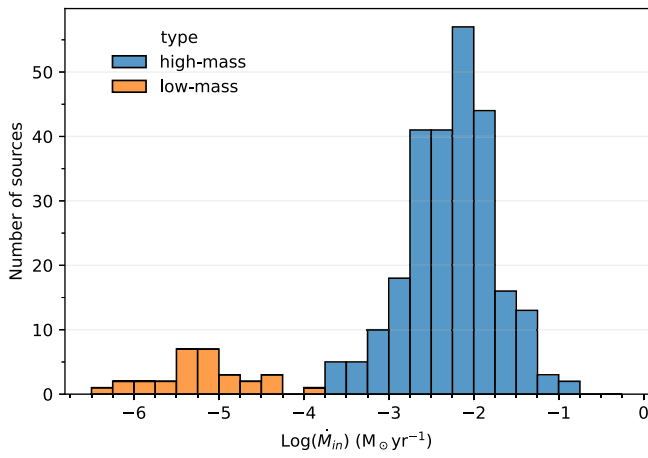


Figure 11. Distribution of mass infall rate provided in the literature.

median values of \dot{M}_{in} at each stage for low-mass cores are $6.03 (\pm 0.41) \times 10^{-6} M_{\odot} \text{yr}^{-1}$ and $6.46 (\pm 0.77) \times 10^{-6} M_{\odot} \text{yr}^{-1}$ respectively, and for high-mass clumps are $2.63 (\pm 0.46) \times 10^{-3}$, $6.76 (\pm 0.41) \times 10^{-3}$, $7.24 (\pm 0.61) \times 10^{-3} M_{\odot} \text{yr}^{-1}$ respectively. Each of them is in the same order of magnitude. We do not find that the mass infall rates of either high-mass or low-mass sources change significantly with evolutionary stages. Note that due to the small number of samples, especially low-mass samples, we need more research to discuss the trend. In addition, the error of distance may also have some influence on the statistical results.

3.7. Association with Masers and Outflows

Infall motion is a part of the initial activity of star formation, and maser is also a common phenomenon in star-forming

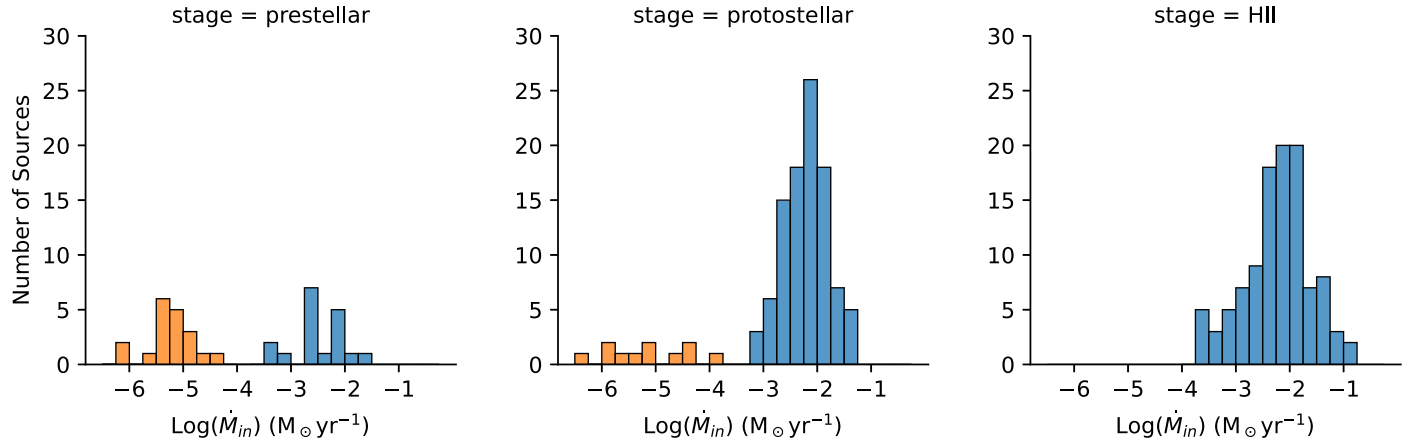


Figure 12. Distribution of mass infall rate for sources at different evolutionary stages. Orange represents low-mass cores and blue represents high-mass clumps.

Table 4
The Maser Association Rate of Sources with Different Masses

		CH ₃ OH-I	CH ₃ OH-II	H ₂ O	OH	maser ^a					
infall sources	high-mass (352)	121	34%	116	33%	151	43%	70	20%	190	54%
	low-mass (54)	7	13%	0	0%	8	15%	2	4%	10	19%
	unknown (50)	2	4%	6	12%	6	12%	3	6%	8	16%
	total (456)	130	29%	122	27%	165	36%	75	16%	208	46%

Note.

^a indicates the number of masers detected in any of the four kinds of masers.

regions. Class I CH₃OH masers are usually associated with outflow because of the collisional pumping mechanism, while class II CH₃OH masers generally occur in compact regions and possibly associated with massive star-forming regions due to the mechanism of radiative pumping. In order to study the correlation, we matched the summarized infall sources with the existing maser database (<https://maserdb.net>).

If a master source is found within 1' of the infall source, we think that they are associated. Table 4 gives the association rate between sources and masers with different types of mass. There are 208 sources being associated with masers, the association rate is 46%, and the number for high-mass and low-mass sources are 190 of 352 (54%) and 10 of 54 (19%), respectively. The number associated with masers of Class I CH₃OH, Class II CH₃OH, H₂O, and OH are 130 (29%), 122 (27%), 165 (36%), 75 (16%), respectively. We find that the association rates between high-mass sources and the four kind of masers are generally greater than those of low-mass. This may indicate the star formation activity near massive sources is more intense. In addition, we can see that there are no low-mass sources associate with class II CH₃OH maser, which is consistent with the conclusion that the class II CH₃OH maser is only associated with the massive star-forming region. Of the four masers, the association rate of H₂O is slightly higher, and that of OH is

lower for both high-mass and low-mass sources. This may be related to the fact that the samples are not unbiased.

In the early stages of star formation, collapse and infall motion are often accompanied by molecular outflows (Li et al. 2014). The study of the relationship between infall and outflow is helpful to better understand the activity mechanism of star formation. Therefore we also matched these sources with outflows provided in some literature (Wu et al. 2004; Maud et al. 2015; Li et al. 2019; Zhang et al. 2020) in the range of 2'. There are 52 (11%) sources being associated with outflows, which is shown in Table A.1 in the Appendix. Part of the reason for the low association rate may be that the outflow samples are incomplete.

4. Summary

We searched the literature related to infall study since 1994, summarized infall sources and made some statistics on the physical properties. The result is summarized below.

1. A total of 456 sources have been cataloged, including 352 (77%) sources with high mass, 55 (12%) with low mass, and the remaining 49 (11%) cannot be categorized. We further divide the high-mass sources into three groups according to the evolutionary stage, that is prestellar,

- protostellar, H II region. The number in the groups are 48 (11%), 215 (47%), 125 (27%), respectively. The remaining 69 (15%) sources have no evolutionary information. Most of the sources are located within 5 kpc from the Sun. We divide the sources into clumps and cores according to their sizes. Vast majority (97%) of the high-mass sources are clumps, and most (85%) of the low-mass sources are cores. Although the current observations are far from complete, the present evidence shows that the star formation activity within the solar circle is more intense than the outer. We summarized the optically thick lines utilized to identify the infall signatures. About 77% of infall sources are identified with HCO^+ (1-0), suggested this line is more effective in identifying infall sources than the others.
2. The H_2 column densities of high-mass clumps ranges between 10^{22} and 10^{24} cm^{-2} , and those of low-mass cores are about 10^{21} cm^{-2} . The median value of high-mass clumps is $4.8 \times 10^{22} \text{ cm}^{-2}$, which is one order of magnitude higher than that of low-mass cores.
 3. We counted the skewness of sources and classified them according to different mass and evolutionary stages, but it does not show significant differences with the mass and evolutionary stage.

4. The median value of infall velocities (V_{in}) for high-mass clumps is 1.12 km s^{-1} with the rms 1.02, and the V_{in} of nearly all low-mass cores are less than 0.5 km s^{-1} . There is no evidence that infall velocity changes with evolution.
5. The range of mass infall rates for low-mass cores are $10^{-7} \sim 10^{-4} M_{\odot} \text{yr}^{-1}$, and for high-mass clumps are $10^{-4} \sim 10^{-1} M_{\odot} \text{yr}^{-1}$ with one exception. We do not find that the mass infall rates change with evolutionary stages for either high-mass or low-mass sources.
6. There are 208 (46%) sources being associated with masers within an angular radius of $1'$. The number of infall sources being associated with masers of Class I CH_3OH , Class II CH_3OH , H_2O , OH are 130 (29%), 122 (27%), 165 (36%), 75 (16%). There are 52 (11%) sources being associated with outflows within $2'$.

Acknowledgments

This work is supported by the National Key R&D Program of China (Grant No. 2017YFA0402702), and the National Natural Science Foundation of China (NSFC, Grant Nos. 11873093 and U2031202). Z.C. acknowledges the support from the NSFC (Grant No. 11903083).

Table A.1
An Excerpt of the Physical Properties of Infall Sources

No.	R.A.	Decl.	Alias	Dist.	V_{LSR}	$N(\text{H}_2)$	$n(\text{H}_2)$	Mass	Lines	δv	V_{in}	\dot{M}_{in}	Type	Stage	Maser	Outflow	Reference	
1	35:40.1	+66:14:23	G121.34+3.42	0.7	-5.3	9.80E+21			1,9	-0.47							3	
2	36:47.5	+63:29:01	G121.30+0.66	1.69	-17.6				2	-0.54			high	123	Y	19		
3	36:53.6	+63:28:03	G121.31+0.64	1.7	-17.3	1.70E+22			1,9	-0.63	0.29	1.60E-03		2		Y	3	
4	52:25.1	+56:33:54	G123.07-6.31	2.53	-30.4				1,2,10	-0.2			high	3	123	Y	19,20	
5	19:51.8	+61:03:26	G133.42+0.00	1.46	-15.2	4.80E+21			9	-0.59				2			3	
6	27:03.8	+61:52:25	W3(OH)	1.96	-48		6.00E+06		1,10	-0.23	0.06	3.00E-04	high	3	1234	Y	14,15,19,20	
†7*	27:04.7	+61:52:26	W3(H ₂ O)	1.96	-47.8	2.60E+24	1.00E+08	2.60E+01	2,10	-0.65	2.7	2.30E-03	high	2	1234	Y	9	
†8	53:12.2	+68:55:52	LDN 1355	0.55	-3.8	1.40E+21	9.10E+03		11	-0.42	0.12	8.40E-06	low	1			6,24	
†9	26:37.0	+30:15:26	IRAS03235	0.25	4.9				2	-0.66			low	2	3		25	
			+3004															
†10	28:32.5	+31:11:05	J03283258	0.24	7.2				9	-0.45	0.17	6.50E-06	low	2			26	
			+3111040															
†11	28:44.5	+31:05:40	IRAS03256	0.24	7.4				11	-0.31			low	2			22	
			+3055															
†12*	29:10.5	+31:13:32	NGC 1333-4A	0.24	7				1,10E+00	2,3,8,11,12	-0.39	0.68	1.10E-04	low	2	13	Y	22,23,30
†13*	29:12.0	+31:13:09	NGC 1333-4B	0.24	7.1				4.80E-01	2,3,8,11,12	-0.34	0.47	4.00E-05	low	2	13	Y	22,23,30
†14	30:32.6	+30:26:26	J0330326	0.25	6.1				9	-1.11	0.06	3.10E-06	low	2			26	
			+302626															
†15	33:54.9	+58:08:19	G143.04+1.76	0.51	-8.8	9.60E+21			1,9	-0.34							3	
†16	10:51.5	+25:09:58	LDN 1498	0.23	7.8	2.80E+21	1.80E+04		11	-0.6	0.03	9.00E-07	low	1			6,24	
†17	18:40.2	+28:29:25	J0418402	0.23	7.3				9	-0.59	0.03	3.50E-07	low	2			26	
			+282925															
†18	18:41.8	+28:23:50	LDN 1495A-S	0.23	7.4	2.20E+21	2.80E+04		11	-0.53	0.07	1.00E-05	low	1			6,24	
†19	19:40.7	+27:13:11	IRAS04166	0.23	6.4				2	-0.97			low	2		Y	25	
			+2706															
†20	28:38.9	+26:51:35	LDN 1521F	0.23	6.5				2,9	-1.12	0.03	1.70E-06	low	2			26,31	
†21	30:14.9	+36:00:08	J0430149	0.28	-0.8				9	-0.77	0.12	1.10E-06	low	2			26	
			+360008															
†22	32:48.7	+24:25:12	TMC2	0.23	6.4	4.50E+21	2.30E+04		11	-0.23	0.17	4.00E-05	low	1			6,24	
†23	39:35.0	+25:41:47	TMC-1A	0.23	6				2	-1.02			low	2		Y	25	
†24	39:53.6	+26:03:06	LDN 1527	0.23	5.9				2,3,12	-0.99			low	2		Y	22	
†25	41:33.0	+25:44:44	TMC1	0.23	5.8	6.90E+21	6.30E+03		11	-0.53	0.05	6.00E-06	low	1			6,24	
†26	47:13.1	+53:03:57	G154.05+5.08	0.26	4.3	3.10E+21			1	-1.91							3	
†27	04:14.9	+25:11:08	LDN 1544	0.23	7.2	8.00E+21	1.40E+04		11	-0.36	0.02	9.00E-07	low	1			6,24	
†28	17:36.0	+25:05:18	LDN 1552	0.23	7.8	3.80E+21	2.30E+04		11	-0.46	0.12	8.10E-06	low	1			6,24	
29	35:50.9	+36:10:41	G172.77+2.09	1.69	-15.3	6.00E+21			1	-0.62	0.04			2			3	
30	41:00.0	+35:48:04	SH 2-235N	1.68	-19.6				1	-0.43			high				20	
31	52:12.1	+26:59:35	IRAS05490	4.42	0.8				1	-0.53			high	2	3	Y	27	
			+2658															
†32	54:38.8	+01:53:44	LDN 1622A-2	0.42	1.2	5.10E+21	3.00E+03		11	-0.11	0.09	1.20E-05	low	1			6,24	
†33*	58:13.5	+16:31:58	G192.16-3.84	1.55	6	2.70E+24		10.8(4.8)	2,14		2	4.70E-03	high	2	3	Y	7	
34	07:41.5	+20:39:44	G189.67+0.17	2.1	7.3	2.50E+22			9	-0.1				2			3	
35	10:51.0	-06:11:50	G213.88-11.84	0.84	10				1				high	3	13	Y	14,18	
36	12:53.6	+17:59:27	J06125362	1.69	9				1		0.8		high	3	123	Y	14,15	
37	12:53.6	+18:00:26	G192.5840-00.0411	1.69	9	4.00E+05			1		0.9	2.00E-04	high	3	123	Y	14,15	
†38*	12:54.0	+17:59:23	SH 2-255IR SMA1	1.67		9.80E+24	6.60E+09	1.64	16		2.5	2.30E-04	high	2	123	Y	4	
39	14:25.2	+17:43:20	G193.01+0.14	1.68	7.9	1.70E+22			9	-0.17		6.00E-04		2		Y	3	
40	59:14.3	-03:54:35	G217.30-0.05	2.56	26.6	2.60E+22			1	-0.25		5.10E-03		2	3	Y	3	
41	44:51.9	-24:07:40	IRAS 07427-2400	5.06	68				1				high	3	34	Y	14,15	
42	03:32.8	-48:28:10	IRAS09018-4816	3.8	10.4		3.90E+05	1.00E+03	6	-0.61	3.41	4.80E-02	high	3	123		1	

Table A.1
(Continued)

No.	R.A.	Decl.	Alias	Dist.	V_{LSR}	$N(\text{H}_2)$	$n(\text{H}_2)$	Mass	Lines	δv	V_{in}	M_{in}	Type	Stage	Maser	Outflow	Reference
43	27:36.5	-62:51:26	G300.218-0.111	4.13	-40	3.90E+22	1.10E+04	7.40E+02	1,7	-0.31	0.51	1.90E-03	high	2			12
44	43:31.0	-62:36:24	G302.021+0.251	4.32	-46	4.50E+22	1.80E+04	6.90E+02	1	-0.42	1.23	5.00E-03	high	3	3		12
45	54:16.0	-61:37:23	G303.268+1.247	1.8	-30.4	1.90E+22	6.70E+03	1.00E+03	1	-0.41	0.51	1.90E-03	high				12
46	05:39.1	-62:14:39	G304.586+0.582	1.74	-22.3	1.70E+22	3.00E+05	4.30E+01	1	-0.29	0.41	6.70E-04	high	3			12
47	06:33.2	-62:33:49	G304.672+0.257	3.5	-43.2	2.80E+22		3.20E+02	1,7	-0.65	1.25		high	2			12
†48	07:36.1	-77:00:05	BHR 86	0.15	3.8				11,12	-0.4			low	2			22
49	08:11.6	-62:10:20	G304.886+0.636	2.82	-36.3	4.80E+22	7.80E+04	3.00E+02	1	-0.38	0.44	1.70E-03	high	2	23		12
50	16:43.1	-62:58:30	IRAS13134-6242	4.14	-32.2		2.80E+04	1.30E+03	6	-0.31	1.99	1.40E-02	high	3	1234		1
51	16:48.4	-62:50:36	G305.822-0.114	3.62	-41.5	5.80E+22	2.90E+04	8.30E+02	1,7	-0.54	1.3	7.10E-03	high	2	123		12
52	39:54.3	-61:41:09	G308.646+0.647	3.72	-46.6	4.20E+22	6.90E+03	6.60E+02	1	-0.65	1.44	4.20E-03	high	3	3		12
53	40:54.0	-61:46:49	G308.744+0.532	3.23	-47	2.10E+22	9.50E+03	2.80E+03	1	-0.26	0.54	4.60E-03	high	3			12
54	41:53.0	-62:07:32	G308.791+0.171	5.01	-50.5	1.90E+22	1.40E+04	9.30E+02	1	-0.69	0.9	4.20E-03	high	3			12
55	43:01.4	-62:08:56	G308.917+0.122	5.01	-50	3.80E+22	4.20E+03	1.60E+03	1	-0.28	0.94	4.20E-03	high	3	234		12
56	45:51.1	-62:33:42	G309.154-0.349	4.44	-40.9	2.50E+22	4.40E+04	5.80E+02	1,7	-0.48	1.24	6.10E-03	high	2			12
57	48:37.9	-62:46:12	G309.421-0.621	2.7	-42.5	7.20E+22	1.10E+04	1.40E+03	1,7	-0.48	0.94	5.30E-03	high	3			12
58	50:55.0	-61:44:21	G309.911+0.324	4.59	-59.4	9.50E+22	1.40E+04	3.20E+03	1,7	-0.39	0.84	8.90E-03	high	2	13		12
59	51:03.7	-61:30:25	G309.981+0.546	2.56	-40.9	3.90E+22	2.70E+04	4.80E+02	1,7	-1.9	1.33	4.90E-03	high	3			12
60	51:13.1	-61:32:34	G309.991+0.507	2.56	-41	2.50E+22	8.70E+04	4.30E+02	1,7	-0.47	0.6	3.00E-03	high	2			12
61	51:38.4	-61:39:15	G310.014+0.387	4.41	-41.1	8.10E+22	1.30E+04	9.10E+02	1	-0.31	0.62	2.80E-03	high	3			12
62	56:01.1	-62:14:20	G310.374-0.304	4.4	-52.6	5.90E+22	1.50E+04	1.80E+03	1	-0.26	0.59	4.30E-03	high	2	1		12
63	03:34.4	-61:15:47	G311.492+0.404	4.36	-58.6	2.60E+22	5.80E+04	6.90E+02	1	-0.52	1.01	6.10E-03	high	3			12
64	08:42.3	-61:10:43	G312.108+0.309	4.03	-47.9	5.40E+22	8.00E+03	9.80E+02	1,7	-1.06	2.43	9.60E-03	high	3	2		12
65	26:04.4	-60:40:54	G314.264+0.091	3.74	-51.3	7.90E+22	9.10E+03	2.00E+03	1,7	-0.37	0.96	6.50E-03	high	3			12
66	42:02.7	-60:30:36	G316.139-0.506	3.73	-60	6.00E+22	3.70E+03	4.90E+03	1,7	-0.6	1.22	1.10E-02	high	3			12
67	42:02.8	-60:30:35	IRAS14382-6017	3.74	-60.2		3.50E+03	4.00E+03	6	-0.6	2.04	1.50E-02	high	3			1
68	42:12.2	-60:41:09	G316.084-0.674	2.34	-38.9	2.80E+22							high	2			12
69	53:42.8	-59:08:57	IRAS14498-5886	3.38	-49.8		1.00E+04	1.00E+03	6	-0.66	3.77	1.60E-02	high	3	1234		1
70	03:39.5	-57:39:30	G319.899+0.791	2.32	-42.8	2.10E+22	5.80E+03	4.50E+02	1,7	-0.41	0.88	1.90E-03	high	3			12
71	05:22.5	-57:27:06	G320.201+0.859	2.34	-41	3.40E+22	1.70E+04	6.60E+02	1,7	-0.56	1.07	4.20E-03	high	3			12
72	07:21.3	-57:49:28	G320.247+0.404	1.51	-32.7	7.80E+22	7.10E+03	7.80E+02	1	-0.28	0.51	1.70E-03	high	3			12
73	11:54.9	-58:09:58	G320.596-0.196	3.3	-52.2	4.70E+22	1.80E+04	3.70E+02	1	-0.43	0.91	2.50E-03	high	3	4		12
74	30:57.1	-56:15:03	G323.799+0.017	3.27	-58.3	2.70E+22	1.40E+04	1.40E+03	1	-0.64	1.54	9.50E-03	high	2	2		12
75	39:10.7	-54:55:43	G325.514+0.414	3.01	-45.8	3.00E+22	1.30E+04	2.60E+03	1,7	-0.49	0.92	8.20E-03	high	3			12
†76	43:01.4	-34:09:12	B228	0.15	5.4				2	-0.74			low	2			25
77	43:33.2	-53:55:28	G326.626+0.834	2.92	-38	6.30E+22	2.90E+04	5.10E+02	1	-0.3	0.62	2.40E-03	high	2			12
78	46:21.1	-54:10:42	G326.796+0.382	1.27	-20.7	6.60E+22	3.00E+04	1.60E+02	1	-0.57	0.84	1.60E-03	high	2			12
79	49:08.2	-54:23:07	G326.987-00.031	3.17	-58.2		2.60E+03	1.00E+03	1,7	-0.53	1.8	4.90E-03	high	2	12		28
80	50:19.0	-53:57:05	G327.393+0.199	6.05	-89.1	1.00E+23	1.20E+04	2.30E+03	1	-0.27	0.79	6.30E-03	high	2	123		12
†81	54:01.1	+02:34:47	LDN 183	0.22	2.6	4.40E+21	2.70E+04		11	-0.06	0.05	9.80E-06	low	1			6,24
82	55:48.8	-52:43:06	IRAS15520-5234	2.88	-41.7		2.20E+04	1.60E+03	6	-0.46	4.33	3.10E-02	high	3	1234		1
83	56:01.7	-53:09:45	G328.549+0.271	3.16	-58.8	3.20E+22	4.20E+04	3.20E+02	1,7	-0.42	0.94	3.00E-03	high	2	1		12
84	56:35.7	-54:14:41	G327.918-0.612	2.93	-45.8	3.80E+22	6.60E+04	1.90E+02	1,7	-0.58	0.96	2.60E-03	high	2			12
85	58:07.5	-51:43:25	G329.721+1.165	5.03	-77.3	5.60E+22	2.30E+04	1.20E+03	1	-0.33	0.97	6.10E-03	high	2	2		12
86	00:32.0	-53:12:54	G329.029-00.206	2.89	-43.5		1.40E+03	2.80E+03	1,7	-0.64	2.34	8.00E-03	high		1234		28
87	01:33.8	-53:11:13	G329.164-0.286	2.97	-50	5.60E+22	1.20E+04	4.40E+03	1,7	-0.52	1.04	1.30E-02	high	2	12		12
88	01:45.2	-52:40:18	G329.524+0.084	5.44	-88.6	5.20E+22	5.00E+03	3.30E+03	1	-0.28	0.93	7.10E-03	high	3	3		12
89	02:22.7	-53:06:06	G329.312-0.302	4.51	-73.9	4.40E+22	2.40E+04	8.70E+02	1	-0.35	0.64	3.40E-03	high	2			12
90	03:32.3	-53:09:28	IRAS15596-5301	4.85	-74.2		5.50E+03	8.00E+03	6	-0.61	3.33	4.50E-02	high	3	234		1
91	09:52.9	-51:54:55	IRAS16060-5146	5.1	-90.4		1.70E+04	8.00E+03	6	-0.56	3.91	7.70E-02	high	3	1234		1
92	09:58.0	-50:56:20	G331.626+0.526	2.96	-51.4	5.10E+22	8.90E+03	8.10E+02	1,7	-0.34	0.7	2.50E-03	high	3	1		12
93	10:01.6	-50:49:37	G331.709+0.602	4.61	-67.5	1.20E+23	1.40E+04	2.90E+03	1,7	-0.4	1.39	1.40E-02	high	2	12		12
94	10:06.8	-50:50:29	G331.709+0.582	4.56	-66.7	1.20E+23	1.80E+04	1.50E+03	1	-0.8	2.9	2.00E-02	high	2	1		12
95	11:00.0	-51:50:22	IRAS16071-5142	5.05	-86.8		1.20E+04	5.00E+03	6	-0.47	4.59	5.80E-02	high	3	1234		1

Table A.1
(Continued)

No.	R.A.	Decl.	Alias	Dist.	V_{LSR}	$N(\text{H}_2)$	$n(\text{H}_2)$	Mass	Lines	δv	V_{in}	M_{in}	Type	Stage	Maser	Outflow	Reference
96	11:18.3	-52:02:04	G331.034-0.419	4.87	-64.9	7.40E+22	1.30E+04	3.60E+03	1	-0.32	0.97	1.10E-02	high				12
97	11:20.1	-52:02:48	G331.029-0.431	3.91	-64.4	6.50E+22	9.70E+03	3.00E+03	1,7	-0.48	1.45	1.30E-02	high				12
98	11:23.1	-52:01:22	G331.051-0.419	4.85	-65.6	2.80E+22	7.20E+03	1.90E+03	1	-0.31	1.3	7.80E-03	high				12
99	11:27.1	-51:41:57	IRAS16076-5134	5.05	-88.4		4.20E+03	4.00E+03	6	-0.75	6.9	5.40E-02	high	3	1234		1
†100*	11:32.6	-51:34:35	G331.372-00.116	5.05	-87.7	3.00E+23	8.50E+05	1.80E+01	2		1.54	2.00E-03	high	1			2
101	11:59.3	-51:28:14	G331.496-0.079	5.04	-88.1	4.20E+22	9.80E+04	1.10E+03	1	-0.41	1.08	1.00E-02	high	3	1		12
102	12:04.1	-52:00:49	G331.134-0.484	4.15	-68.3	8.50E+22	2.70E+03	6.60E+03	1	-0.26	0.8	7.90E-03	high	3	1		12
103	12:05.9	-51:29:10	G331.498-0.102	5.03	-88	6.50E+22	1.10E+04	2.30E+03	1	-0.49	1.47	1.20E-02	high	3	134		12
104	12:09.9	-51:28:36	G331.512-0.102	5.03	-88.9	2.20E+23	2.40E+04	4.90E+03	1,7	-0.56	2.2	3.70E-02	high	3	1234		12
105	12:27.0	-51:43:32	G331.374-0.314	5.05	-97	2.80E+22			1,7	-0.52	1.1		high	2			12
106	13:00.0	-51:31:43	G331.571-0.229	2.96	-50.3	3.60E+22	1.10E+04	3.20E+02	1,7	-0.3	0.51	1.10E-03	high	2			12
107	15:17.4	-50:55:60	G332.241-0.044	2.91	-47.7	8.70E+22	7.80E+03	1.80E+03	1	-0.65	1.84	1.10E-02	high	2	1		12
108	15:24.1	-50:55:59	G332.254-0.056	2.92	-48.3	3.70E+22	3.10E+04	6.90E+02	1,7	-0.48	0.89	4.40E-03	high	2	1		12
109	15:34.1	-50:55:43	G332.276-0.071	2.91	-48	2.10E+22	1.10E+04	4.70E+02	1,7	-0.99	1.42	3.80E-03	high	2			12
110	15:45.7	-50:55:53	G332.296-0.094	2.93	-49	1.50E+23	6.80E+03	1.70E+03	1	-0.67	1.57	8.60E-03	high	3	123		12
111	16:42.9	-50:50:17	G332.469-0.131	2.95	-50.2	2.30E+22	8.10E+03	4.70E+02	1	-0.41	0.54	1.30E-03	high	3			12
112	17:11.6	-50:47:13	G332.559-0.147	2.9	-46.8	2.80E+22	1.70E+04	7.90E+02	1	-0.28	0.44	2.00E-03	high	2	2		12
113	17:29.2	-50:46:12	G332.604-0.167	2.9	-46.5	4.60E+22	3.60E+03	1.50E+03	1,7	-0.73	1.78	7.30E-03	high	2	123		12
114	19:48.0	-51:02:18	G332.677-0.614	3.29	-57.7	8.70E+22	6.10E+03	1.10E+04	1,7	-0.46	1.07	1.90E-02	high	3			12
115	20:07.2	-50:04:50	G333.386+0.032	4.76	-70.3	3.90E+22	8.80E+03	3.10E+03	1,7	-0.5	1.27	1.10E-02	high	3	1234		12
116	20:26.4	-50:41:43	G332.990-0.441	3.03	-55.5	8.10E+21	3.60E+03	1.30E+02	1	-0.52	0.34	2.60E-04	high	3	13		12
117	20:29.3	-50:33:44	G333.089-0.352	2.97	-52.5	1.40E+22	3.70E+03	3.00E+02	1	-0.29	0.65	8.90E-04	high	3			12
118	20:34.2	-50:51:19	G332.892-0.569	3.12	-57	1.30E+22	1.20E+04	3.80E+02	1	-0.44	0.93	2.20E-03	high	1			12
119	20:43.2	-50:37:04	G333.076-0.417	2.99	-54.4	4.40E+22	2.30E+04	7.60E+02	1,7	-0.29	0.52	2.50E-03	high				12
120	21:20.4	-50:11:17	G333.449-0.182	2.86	-44.2	3.50E+22	3.10E+04	4.70E+02	1,7	-0.45	1.65	6.20E-03	high	1	2		12
121	21:21.8	-50:49:46	G332.999-0.639	2.92	-48	1.40E+22	4.50E+03	2.30E+02	1,7	-0.8	1.66	2.10E-03	high	2			12
122	22:03.3	-50:11:48	G333.524-0.269	2.93	-49.5	6.00E+22	3.10E+03	2.50E+03	1,7	-0.49	1.1	5.80E-03	high	1	1		12
123	22:38.9	-50:01:39	G333.711-0.217	2.9	-47.3	1.50E+22	3.30E+04	1.60E+02	1	-0.61	1.13	2.20E-03	high	2			12
124	23:43.4	-48:52:37	G334.651+0.469	4.55	-65.4	1.90E+22	8.20E+03	8.50E+02	1,7	-0.81	1.08	3.90E-03	high	2			12
†125	26:26.4	-24:24:30	VLA 1623	0.16	3.7				11,12	-0.64			low	2	3	Y	22
126	26:55.4	-48:25:03	G335.349+0.412	4.49	-59.4	2.20E+22	6.70E+04	6.80E+02	1	-0.62	0.98	6.20E-03	high	2			12
†127	26:59.0	-24:34:57	WL 22	0.16	3.8				11,12	-0.99			low	2			22
128	27:26.8	-49:12:39	G334.838-0.201	2.87	-45	2.50E+22	6.70E+03	1.90E+02	1	-0.46	0.65	8.30E-04	high	3			12
129	28:51.2	-48:50:41	G335.262-0.114	2.85	-44.1	3.00E+22	2.30E+04	7.60E+02	1,7	-1.27	1.79	8.50E-03	high	2			12
130	29:03.6	-48:59:41	G335.177-0.242	2.86	-45.6	1.30E+22	6.50E+03	5.50E+02	1,7	-1.11	0.92	2.30E-03	high	3			12
131	30:59.1	-48:43:53	IRAS16272-4837	2.88	-46.6		1.10E+04	1.60E+03	6	-0.4	2.58	1.50E-02	high	3	1234	Y	1
132	30:59.2	-48:43:53	G335.586-0.291	2.89	-46.9	3.40E+23	1.30E+04	3.30E+03	1	-0.27	0.73	7.60E-03	high	3	1234	Y	12
†133	31:26.8	+24:15:54	IRAS16293-2422	0.07	4				2,3,11,12				low	2			22
†134	33:49.1	+24:25:28	LDN 1689B	0.07	4	1.80E+21	2.50E+04		11	-0.29	0.05	4.90E-06	low	1			6,24
135	34:13.3	-48:06:14	G336.411-0.256	4.49	-87.6	6.50E+22	2.00E+03	5.90E+03	1	-0.3	1.17	9.60E-03	high	3	12		12
136	36:17.1	-47:40:44	G336.958-0.224	4.39	-71.6	4.60E+22	3.90E+03	6.30E+03	1,7	-0.56	1.44	1.60E-02	high		23		12
137	36:18.8	-47:23:19	G337.176-0.032	4.39	-68.4	7.40E+22	4.40E+03	3.60E+03	1,7	-0.42	1.42	1.10E-02	high	2	23		12
138	36:56.4	-47:22:27	G337.258-0.101	4.38	-68.2	7.40E+22	3.70E+03	1.20E+04	1,7	-0.44	1.38	2.20E-02	high	2	234		12
139	38:29.6	-47:00:41	IRAS16348-4654	2.8	-46.9		7.50E+03	2.50E+04	6	-0.51	1.81	5.80E-02	high	3	1234		1
140	38:51.0	-47:27:58	IRAS16351-4722	2.69	-40.2		2.00E+04	1.60E+03	6	-0.76	3.02	2.10E-02	high	3	1234		1
141	38:58.0	-47:07:41	G337.671-0.192	2.94	-51.6	4.20E+22	1.30E+04	5.00E+02	1	-0.34	0.85	2.50E-03	high	3			12
142	39:48.5	-47:12:41	G337.704-0.354	2.72	-41.6	9.30E+21	1.80E+03	4.00E+03	1	-0.45	0.94	5.80E-03	high	3			12
143	39:57.9	-47:09:31	G337.761-0.339	2.72	-41.8	9.10E+22	1.30E+04	2.10E+03	1,7	-0.39	1.08	8.30E-03	high	2			12
144	39:58.2	-48:02:46	G337.098-0.929	2.67	-41.8	3.50E+22	1.50E+04	3.70E+02	1,7	-0.64	1.28	3.20E-03	high	2	2		12
145	40:13.8	-45:38:30	G338.926+0.634	4.55	-61.8	9.10E+22	4.60E+03	2.10E+03	1,7	-0.88	3.2	1.70E-02	high	2	2		12
146	40:27.1	-47:07:16	G337.844-0.376	2.7	-40	5.00E+22	2.80E+03	5.40E+03	1	-0.31	0.5	4.30E-03	high	3	2		12
148	40:50.9	-46:27:37	G338.384+0.011	2.67	-32.2	7.90E+22	7.10E+03	1.50E+03	1	-0.6	2.45	1.30E-02	high	3			12
147	40:50.9	-46:23:27	G338.436+0.057	2.57	-38.9	1.70E+22	1.30E+04	3.30E+02	1	-0.46	1.29	2.90E-03	high		23		12

Table A.1
(Continued)

No.	R.A.	Decl.	Alias	Dist.	V_{LSR}	$N(\text{H}_2)$	$n(\text{H}_2)$	Mass	Lines	δv	V_{in}	M_{in}	Type	Stage	Maser	Outflow	Reference
149	41:01.3	-47:05:46	G337.927-0.432	2.68	-39.1	1.50E+22	1.00E+03	7.10E+02	1	-0.43	1.34	2.10E-03	high				12
150	41:10.6	-47:08:03	G337.916-0.477	2.68	-38.8	3.20E+23	2.00E+04	1.90E+03	1,7	-0.49	1.29	1.10E-02	high	2	1234		12
151	41:16.5	-45:48:57	G338.916+0.382	2.55	-24.5	6.20E+22	3.50E+03	1.60E+04	1	-0.47	1.22	2.40E-02	high	3	23		12
152	41:22.7	-47:08:26	G337.934-0.507	2.67	-38.6	6.00E+22	7.00E+03	8.90E+02	1,7	-0.9	2.1	7.50E-03	high	3			12
153	42:28.0	-46:46:50	G338.327-0.409	2.66	-38.2	3.20E+22	1.70E+04	2.00E+02	1	-0.65	1.3	2.30E-03	high	2	12		12
154	44:14.2	-45:31:27	G339.476+0.184	6.1	-92.1	5.50E+22	4.90E+03	3.60E+03	1,7	-0.62	2.15	1.70E-02	high	3	23		12
155	45:05.9	-45:30:19	G339.589+0.082	6.14	-109.7	3.20E+22	2.00E+03	3.50E+03	1,7	-0.57	1.5	8.70E-03	high	3			12
156	45:59.2	-45:38:43	G339.584-0.127	2.61	-34.1	1.10E+23	3.90E+04	7.40E+02	1	-0.78	2.2	1.20E-02	high	2	123		12
†157	46:51.9	+13:47:60	LDN 158	0.19	4	1.50E+21	4.10E+05		11	-0.56	0.07	7.60E-06	low	1			6,24
158	47:03.5	-45:21:31	G339.924-0.084	4.2	-53.1	7.80E+22	2.70E+03	1.30E+04	1,7	-0.42	1.19	1.80E-02	high	2	3		12
†159	47:37.9	+10:38:49	LDN 234E-C	0.22	2.9	1.90E+21	2.80E+05		11	-0.55	0.05	3.30E-06	low	1			6,24
†160	47:44.3	+10:46:54	LDN 234E-S	0.22	3.1	2.60E+21	3.50E+04		11	-0.63	0.05	4.00E-06	low	1			6,24
161	47:56.5	-45:07:15	G340.206-0.049	8.91	-120.9	3.50E+22	5.60E+03	2.10E+03	1,7	-0.5	1.52	8.90E-03	high				12
162	48:13.9	-45:21:46	G340.054-0.244	4.31	-53.1	1.90E+23	4.00E+03	3.20E+03	1,7	-0.46	1.38	9.50E-03	high	3	1234		12
163	48:27.5	-45:09:48	G340.232-0.146	2.92	-50.5	3.10E+22	5.40E+03	9.10E+03	1	-0.62	1.51	2.30E-02	high	2			12
164	48:40.9	-45:15:57	G340.179-0.242	4.32	-53.3	2.70E+22	1.90E+03	1.90E+04	1	-0.33	1.12	2.00E-02	high	1			12
165	48:46.9	-45:10:24	G340.261-0.196	2.76	-43.8	2.60E+22	5.40E+03	8.90E+02	1	-0.49	1.36	4.40E-03	high				12
166	50:14.9	-44:42:32	G340.784-0.097	5.85	-101.4	3.00E+02	3.70E+03	1	-1.14	0.9	3.00E-03	high		1234		28	
167	50:51.6	-44:08:44	G341.287+0.179	2.51	-23.6	2.40E+22	2.40E+04	3.70E+02	1,7	-0.85	1.53	4.60E-03	high	2			12
168	50:53.9	-44:09:28	G341.282+0.166	2.52	-24.3	1.40E+22	1.30E+04	1.30E+02	1	-0.69	1.02	1.20E-03	high	3			12
169	51:44.9	-44:46:39	G340.901-0.346	2.76	-43.1	2.10E+22	5.30E+04	3.60E+02	1,7	-1.92	3.03	1.20E-02	high	2			12
170	52:17.8	-44:26:55	G341.217-0.212	2.75	-43.1	1.00E+23	2.40E+04	6.90E+02	1,7	-0.8	2.08	9.40E-03	high	2	1234		12
171	52:23.2	-43:18:03	G342.114+0.504	2.5	-25.1	2.60E+22	3.00E+04	3.50E+02	1,7	-0.48	0.86	2.70E-03	high	1			12
172	52:27.0	-44:31:03	G341.181-0.277	2.76	-43.7	3.10E+22	6.70E+04	2.30E+02	1,7	-1.17	1.92	5.90E-03	high	2			12
173	52:30.4	-44:28:36	G341.219-0.259	2.77	-44.5	6.50E+22	1.50E+04	1.00E+03	1	-0.58	1.42	7.20E-03	high	2	1		12
174	52:37.1	-44:28:17	G341.236-0.271	2.77	-44.2	8.50E+22	8.60E+03	1.80E+03	1,7	-0.9	2.21	1.40E-02	high	2	12		12
175	52:51.6	-44:28:04	G341.266-0.302	2.75	-43.3	1.00E+23	9.20E+03	1.80E+03	1,7	-0.64	1.69	1.10E-02	high	3			12
176	54:00.5	-43:16:19	G342.323+0.294	5.7	-114.5	2.20E+22	2.90E+03	3.70E+03	1,7	-0.3	0.59	4.10E-03	high	3			12
177	54:39.2	-43:52:14	G341.932-0.174	2.76	-42.8	1.00E+23	1.50E+04	3.90E+03	1	-0.28	0.86	1.00E-02	high	3			12
178	54:39.2	-43:51:28	G341.942-0.166	2.75	-42	1.90E+23	1.70E+04	4.70E+03	1	-0.36	1.21	1.70E-02	high	3			12
179	54:56.8	-45:09:07	G340.969-1.021	2.5	-24.1	2.80E+23	5.80E+04	1.30E+03	1	-0.32	1.03	9.50E-03	high	2	12		12
180	58:17.2	-42:52:02	G343.128-0.062	2.58	-30.8	3.20E+23	2.00E+04	2.10E+03	1,7	-0.43	1.3	1.20E-02	high	3	134		12
181	59:30.8	-42:35:07	G343.489-0.064	2.55	-28.3	3.60E+22	2.40E+03	5.50E+02	1	-0.6	0.92	1.70E-03	high	3	3		12
182	00:33.2	-42:25:08	G343.738-0.112	2.55	-27.5	6.30E+22	1.30E+04	4.40E+02	1,7	-0.66	1.39	3.80E-03	high	2	3		12
183	00:50.1	-42:26:12	G343.756-0.0164	2.55	-26.9	1.30E+03	1.30E+03	1,7	-0.82	0.7	2.00E-03	high		23		28	
184	01:01.3	-42:48:08	G343.489-0.416	2.58	-28.7	4.00E+22	1.50E+04	6.60E+02	1	-0.43	0.57	2.10E-03	high	1			12
185	02:09.1	-41:46:49	G344.424+0.046	4.02	-66.3	1.00E+23	3.10E+03	6.30E+03	1,7	-0.7	1.54	1.50E-02	high	3	234		12
186	03:17.1	-42:25:58	G344.036-0.519	2.68	-24	3.40E+22	6.70E+03	8.50E+02	1	-0.29	0.82	2.80E-03	high	2			12
187	03:26.2	-42:29:41	G344.004-0.579	2.52	-22.8	4.20E+22	3.30E+04	1.10E+03	1,7	-0.64	2.25	1.50E-02	high	2			12
188	03:30.0	-42:37:56	G343.902-0.672	2.58	-29.5	3.30E+22	1.40E+03	1.70E+04	1,7	-0.29	0.7	1.00E-02	high	2			12
189	04:07.1	-42:28:03	G344.102-0.662	2.67	-25.6	7.80E+22	6.70E+03	1.30E+03	1,7	-0.73	2.18	9.90E-03	high	3			12
190	05:23.3	-41:32:50	G344.977-0.292	2.71	-28	2.80E+22	7.70E+04	3.80E+02	1,7	-0.9	1.68	7.50E-03	high	1			12
191	07:53.9	-40:31:39	G346.076-0.056	5.23	-84.1	5.10E+22	2.00E+03	6.50E+03	1	-0.48	1.38	1.20E-02	high	3			12
192	08:01.5	-41:38:39	G345.196-0.744	1.33	-22.3	2.10E+22	3.40E+03	6.20E+03	1,7	-0.61	0.6	6.10E-03	high	3			12
193	11:19.1	-40:38:38	G346.369-0.647	1.31	5.8	3.00E+22	6.30E+03	9.30E+03	1,7	-1.42	0.49	8.10E-03	high	2			12
194	12:31.3	-38:19:09	G348.383+0.537	1.3	-7.2	3.90E+22	1.50E+05	2.50E+02	1	-0.48	0.61	2.60E-03	high	1			12
195	12:33.2	-38:19:57	G348.376+0.524	1.3	-7.3	5.80E+22	5.30E+04	2.00E+02	1	-0.41	0.73	1.90E-03	high	2			12
196	14:24.7	-38:32:34	G348.419+0.106	5.06	-104.9	2.00E+22	1.70E+04	1.20E+03	1,7	-0.45	0.91	5.30E-03	high	2			12
197	17:49.1	-36:09:14	G350.757+0.942	1.32	-9.1	6.90E+22	2.90E+03	4.70E+04	1,7	-0.42	0.97	3.60E-02	high	2			12
198	17:58.6	-36:13:23	G350.719+0.876	1.32	-6.5	2.20E+22	2.70E+03	9.80E+03	1	-0.42	0.56	6.60E-04	high	2			12
199	18:27.1	-36:13:33	G350.772+0.796	1.31	-4.7	2.30E+22	2.40E+05	2.30E+01	1	-0.63	0.52	5.20E-04	high	1			12
200	18:28.0	-36:12:47	G350.784+0.801	1.31	-4.4	1.90E+22	6.10E+04	5.80E+01	1	-0.89	0.33	3.90E-04	high	1			12
201	19:05.1	-36:06:42	G350.939+0.757	1.31	-4.2	4.50E+22	1.50E+05	7.10E+01	1,7	-0.64	1.32	2.40E-03	high	2			12

Table A.1
(Continued)

No.	R.A.	Decl.	Alias	Dist.	V_{LSR}	$N(\text{H}_2)$	$n(\text{H}_2)$	Mass	Lines	δv	V_{in}	M_{in}	Type	Stage	Maser	Outflow	Reference
202	19:08.2	-36:06:59	G350.941+0.746	1.31	-3.8	6.00E+22	3.80E+04	1.90E+02	1,7	-0.78	1.51	3.30E-03	high	2			12
203	19:10.5	-39:00:22	G348.579-0.919	2.8	-14.7	9.30E+22	1.50E+04	1.10E+03	1,7	-0.46	1.13	5.90E-03	high	2	1234		12
204	19:11.6	-39:02:21	G348.554-0.941	1.31	-14.3	2.90E+22	1.10E+04	3.50E+02	1	-0.41	1.1	2.40E-03	high				12
205	19:12.2	-38:59:08	G348.599-0.912	2.8	-14.5	6.90E+22	2.00E+05	1.00E+04	1	-0.39	0.89	4.90E-02	high	2	3		12
206	19:18.2	-39:04:48	G348.533-0.982	1.31	-14.6	1.10E+23	2.70E+04	1.40E+04	1	-0.31	0.85	3.00E-02	high	3	234		12
207	19:20.3	-39:03:54	G348.549-0.979	2.78	-16.1	1.70E+23	1.20E+04	6.30E+02	1	-0.31	0.87	2.90E-03	high	3	1234		12
208	19:26.8	-37:11:01	IRAS17160-3707	4.97	-70		1.10E+04	1.30E+04	6	-0.47	1.66	3.80E-02	high	3	234		1
209	20:15.4	-35:59:29	G351.173+0.632	1.32	-5	6.50E+22	4.60E+03	4.80E+02	1	-0.33	0.78	1.60E-03	high				12
210	20:48.8	-35:45:07	G351.434+0.676	1.31	-3.3	1.90E+23	1.50E+05	4.40E+02	1	-0.26	0.73	4.40E-03	high				12
211	20:54.6	-35:45:13	G351.444+0.659	1.32	-4.2	8.30E+23	1.10E+05	3.40E+03	1	-0.31	1.08	2.30E-02	high	2	123	Y	12
212	20:56.1	-37:00:52	G350.411-0.064	2.76	-27	5.40E+22	3.70E+03	1.40E+04	1,7	-0.39	0.9	1.60E-02	high	2	13		12
213	21:59.6	-35:27:43	G351.809+0.644	1.31	-2.2	4.00E+22	9.50E+04	7.20E+01	1	-0.61	0.78	1.20E-03	high	2			12
214	22:25.4	-37:05:10	G350.521-0.349	2.77	-22.7	5.10E+22	5.00E+03	1.10E+03	1	-0.4	0.86	3.20E-03	high	2	23		12
215	23:16.3	-34:48:47	G352.492+0.796	1.32	-2.9	1.20E+23	3.20E+04	1.40E+02	1	-0.33	0.74	1.30E-03	high	3			12
216	23:20.9	-34:48:42	G352.502+0.784	1.32	-1.6	5.20E+22	1.90E+05	3.80E+01	1	-1.01	1.89	2.50E-03	high	2			12
217	23:24.3	-34:48:31	G352.511+0.776	1.31	-1.2	3.50E+22	2.30E+04	2.60E+01	1,7	-0.74	1.27	6.30E-04	high	1			12
218	23:50.3	-36:38:58	IRAS17204-3636	2.7	-17.7		1.50E+04	7.90E+02	6	-0.83	1.21	4.90E-03	high	3			1
219	23:50.4	-36:38:59	G351.041-0.336	2.71	-18.5	1.10E+23	1.70E+04	7.60E+02	1,7	-0.37	1.05	4.50E-03	high	3			12
220	24:50.8	-34:10:21	G353.204+0.889	1.32	-2.6	4.20E+22	6.00E+02	2.30E+04	1	-0.34	0.32	2.60E-04	high	3			12
221	25:25.0	-36:12:45	IRAS17220-3609	5.96	-94.9		5.90E+03	2.00E+04	6	-0.77	4.71	1.20E-01	high	3	1234		1
222	25:39.4	-34:31:04	G353.012+0.557	1.32	-0.7	3.30E+22	4.90E+04	1.00E+01	1,7	-0.67	1.7	5.80E-04	high	2			12
223	25:54.3	-34:32:25	G353.022+0.502	1.32	-3.6	3.50E+22	4.90E+03	3.00E+02	1	-0.4	1.11	1.70E-03	high				12
224	26:03.4	-34:16:19	G353.262+0.626	1.32	-4.2	2.50E+22	1.50E+05	2.20E+01	1,7	-0.64	0.72	6.00E-04	high				12
225	26:04.5	-35:30:00	G352.246-0.064	4.87	-90.6	1.40E+22	2.10E+03	4.50E+03	1,7	-0.27	0.66	4.60E-03	high	3			12
226	26:13.5	-34:31:54	G353.066 +00.452_2	1.32	1.9		2.00E+03	2.00E+02	1,7	-0.63	1.2	1.10E-03	high	2			28
227	26:19.2	-34:31:01	G353.089+0.444	1.32	-1.8	4.50E+22	2.30E+04	6.00E+01	1,7	-0.52	1.02	9.00E-04	high	3			12
228	26:24.9	-35:34:15	G352.226-0.161	4.85	-90.2	1.40E+22		7.80E+02	1,7	-0.63	1.75		high	3			12
229	26:26.9	-35:33:39	G352.238-0.161	4.86	-91.8	3.20E+22	1.80E+03	1.60E+03	1	-0.39	0.98	3.20E-03	high	2			12
230	26:46.8	-33:59:26	G353.579+0.659	1.31	-1.1	4.50E+22	4.90E+04	2.30E+01	1,7	-0.64	1.09	6.50E-04	high	2			12
231	29:13.6	-34:32:53	G353.396-0.071	4.82	-49.6	9.80E+22	5.90E+03	4.30E+03	1	-0.31	1.21	1.20E-02	high	3			12
232	30:17.3	-33:13:51	G354.616+0.472	3.73	-20.3	1.90E+23	1.60E+04	2.60E+03	1,7	-0.29	0.78	7.40E-03	high	3	1234		12
233	30:33.8	-33:50:24	G354.139+0.089	4.82	-87.7	2.10E+22	8.00E+03	1.90E+03	1	-0.59	0.66	4.10E-03	high	2			12
234	33:50.5	-32:46:01	G355.412+0.102	1.32	4.8	6.20E+22	4.70E+03	1.80E+04	1	-0.35	0.81	1.90E-02	high	2	1		12
235	34:40.5	-33:48:42	G354.629-0.611	1.32	-2.9	2.40E+22	2.80E+04	1.20E+02	1,7	-0.38	0.78	1.20E-03	high	2			12
236	34:56.7	-33:05:33	G355.264-0.269	1.32	-2.9	8.50E+22	4.40E+04	1.70E+02	1,7	-0.5	1.48	3.20E-03	high	2			12
237	35:03.6	-32:39:48	G355.638-0.057	3.73	-19.8	2.30E+22			1,7	-0.68	2.18		high	2			12
238	35:11.7	-33:30:24	G354.944-0.537	1.32	-5.9	5.10E+22	2.20E+04	2.60E+02	1,7	-0.52	1.06	2.40E-03	high	1			12
239	35:38.5	-33:16:01	G355.196-0.486	1.32	-5.3	3.00E+22	5.60E+04	3.80E+02	1,7	-1.08	0.57	2.30E-03	high	2			12
240	36:14.1	-31:49:12	G356.482+0.189	1.33	-5.5	5.10E+22			1,7	-0.46	0.84		high	2			12
241	36:36.4	-24:11:31	G002.97+4.22	5.21	19.7	1.60E+21			9	-1.75						3	
242	42:15.3	-31:17:45	G357.609-0.617	1.32	2.6	4.40E+22			1	-0.29	0.55		high	2			12
243	42:50.3	-29:45:44	G358.979+0.084	5.93	-2.3	4.80E+22			1,7	-0.63	1.03		high	2	23		12
244	43:23.0	-30:18:48	G358.572-0.306	2.73	-4.3	3.20E+22			1,7	-0.64	1.15		high	1			12
245	43:24.1	-30:17:58	G358.586-0.302	2.73	-4.5	3.00E+22			1	-0.43	1.18		high	1			12
246	44:29.6	-29:42:18	G359.216-0.192	5.33	15.6	1.70E+22			1,7	-0.58	0.5		high	1			12
247	44:32.9	-29:42:45	G359.216-0.206	5.34	15.8	1.90E+22			1,7	-1.05	0.78		high	1			12
248	44:41.2	-28:53:40	G359.929+0.196	2.74	-3.5	4.30E+22			1	-0.66	1.49		high	1			12
249	47:45.4	-29:02:15	G000.156-0.452	2.85	17	4.40E+22			1,7	-0.45	0.94		high	1	23		12
250	47:45.4	-29:01:33	G000.166-0.446	2.85	16.2	6.30E+22			1	-0.29	0.59		high	3	23		12
251	49:24.0	-28:48:46	G000.534-0.644	2.84	16.1	4.50E+22			1	-0.69	1.19		high	2			12
252	49:30.6	-28:53:07	G000.484-0.702	2.83	14.2	5.20E+22			1	-1.56	3.27		high	2	1		12
253	50:20.7	-28:52:12	G000.591-0.851	2.83	17.3	1.90E+22		4.10E+01	1	-0.36	0.94		high	1			12

Table A.1
(Continued)

No.	R.A.	Decl.	Alias	Dist.	V_{LSR}	$N(\text{H}_2)$	$n(\text{H}_2)$	Mass	Lines	δv	V_{in}	M_{in}	Type	Stage	Maser	Outflow	Reference	
254	50:46.1	-26:39:49	G002.534+0.199	2.82	9.7	5.50E+22			1,7	-0.5	1.04		high	2	23		12	
255	53:33.8	-25:19:42	G004.003+0.339	2.94	12.5	3.70E+22	8.20E+03	6.00E+02	1,7	-0.52	0.85	2.50E-03	high	3	3		12	
256	53:35.9	-25:20:19	G003.998+0.327	2.94	12.4	2.50E+22			1	-0.69	0.97		high	3	3		12	
257	54:53.9	-26:11:07	G003.416-0.354	4.71	-25.3	4.90E+22			1	-0.57	1.89		high	1			12	
258	55:46.7	-26:16:47	G003.434-0.572	2.91	2.5	3.20E+22			1	-1.28	1.31		high	1			12	
259	57:48.7	-24:19:15	G005.359+0.014	2.94	12.7	3.10E+22	2.30E+04	2.30E+02	1,7	-0.62	0.78	1.70E-03	high	2			12	
260	58:44.5	-24:08:43	G005.617-0.082	4.67	-26.3	9.10E+22	7.40E+03	2.50E+03	1,7	-0.58	1.71	1.20E-02	high	2	123		12	
261	58:47.7	-25:17:40	G004.627-0.666	2.93	9.9	2.80E+22	3.40E+03	7.90E+03	1,7	-0.86	1.58	1.90E-02	high	2	1		12	
262	00:16.0	-23:59:57	G005.917-0.311	2.94	10.1	1.20E+22	1.30E+04	5.60E+03	1,7	-0.51	0.77	1.10E-02	high	1			12	
263	00:43.7	-24:04:57	G005.897-0.444	2.94	9.7	7.20E+22	1.10E+04	8.30E+02	1,7	-1.24	2.11	8.30E-03	high	3	123		12	
264	00:51.5	-24:10:19	G005.834-0.514	2.94	16.3	5.00E+22	4.20E+03	1.80E+03	1,7	-0.47	0.86	4.10E-03	high	3			12	
265	01:17.6	-22:41:43	G007.166+0.131	6.41	80.9	4.00E+22	1.60E+04	2.70E+03	1	-0.39	1.17	1.10E-02	high	2	123		12	
266	02:02.9	-23:53:13	G006.216-0.609	3.56	18.6	8.10E+22	9.20E+03	1.70E+03	1,7	-0.57	1.27	7.60E-03	high	2	1		12	
267	02:18.8	-22:45:03	G007.234-0.101	3.57	19.1	4.70E+22	1.40E+04	1.70E+03	1,7	-0.44	0.92	6.40E-03	high	1			12	
268	05:22.3	-21:44:37	G008.459-0.222	2.87	37.8	4.00E+22	1.50E+04	6.60E+02	1	-0.7	1.72	6.50E-03	high	2	1		12	
269	05:30.1	-21:49:37	G008.401-0.289	2.87	37.1	6.60E+22	1.00E+04	1.90E+03	7	-0.21	0.51	3.50E-03	high	3	3		12	
270	05:33.1	-21:49:36	G008.407-0.299	2.87	37	4.50E+22			4.30E+02	1	-0.31	0.79		high	2	3		12
271	05:44.4	-21:50:48	G008.411-0.347	2.87	38	3.80E+22	5.80E+03	1.30E+03	1,7	-1.19	1.51	6.60E-03	high	3			12	
272	06:19.0	-21:37:32	G008.67-0.36	2.86	36		1.80E+05		1	-0.44	0.4	4.00E-04	high	3	1234		14,15,19	
273	06:19.2	-21:37:27	G008.671-0.356	2.86	34.8	3.00E+23	1.50E+04	5.20E+03	1,7	-0.38	1.42	2.10E-02	high	3	1234		12	
274	06:23.4	-21:37:05	G008.684-0.367	2.87	37.1	1.30E+23	2.50E+04	3.50E+03	1,7	-0.56	2.63	3.60E-02	high	2	234		12	
275	06:24.8	-21:40:10	G008.642-0.397	2.87	38.9	4.70E+22			7	-0.1	0.19		high	2			12	
276	06:28.8	-21:34:13	G008.736-0.362	2.87	39.4	5.50E+22	8.10E+03	2.10E+03	1	-0.53	1.42	9.50E-03	high	3	3		12	
277	06:36.7	-21:37:19	G008.706-0.414	2.87	39	9.10E+22	1.10E+04	6.30E+03	1	-0.29	0.72	1.10E-02	high	2	3		12	
278	06:49.3	-20:59:13	G009.284-0.147	3.81	41.7	5.20E+22	1.60E+04	2.10E+03	1,7	-0.62	1.15	9.50E-03	high	2			12	
279	08:16.7	-22:05:20	G008.486-0.979	2.91	15.8	4.90E+22	3.80E+04	7.90E+02	1	-0.52	0.82	4.80E-03	high	2	3		12	
280	08:19.6	-22:04:29	G008.504-0.982	1.25	15.3	4.00E+22	6.40E+04	5.90E+02	1	-0.35	0.48	2.70E-03	high	2	3		12	
281	08:38.2	-19:51:49	IRAS18056-1952	7.96	68.5		8.30E+03	2.50E+04	6	-0.59	3.08	1.00E-01	high	3	1234	1		
282	08:38.4	-19:51:52	G10.47+0.03	7.42	67		7.20E+05		1	0.42	1.60E-02	high	3	1234		14,16		
283	08:46.5	-20:05:50	G10.1284-0.114	1.25	14.1	1.10E+23	7.80E+03	2.60E+04	1,7	-0.35	1.19	4.20E-02	high	2	123		12	
284	08:49.2	-20:05:54	G10.1288-0.124	1.25	13.9	8.50E+22	1.20E+05	5.80E+02	1,7	-0.3	0.81	5.50E-03	high	3	123		12	
285	09:20.8	-20:02:03	G010.404-0.201	1.25	11.5	4.40E+22	4.50E+03	3.00E+04	1,7	-1.2	1.53	4.90E-02	high	3	3		12	
286	09:21.1	-20:16:10	G010.199-0.316	1.25	11.2	3.00E+22			1,7	-0.64	2.63		high	1	1		12	
287	10:05.7	-19:26:46	G011.004-0.071	2.85	28.4	4.80E+22	5.40E+04	1.00E+03	1,7	-1.22	1.77	1.40E-02	high	2			12	
288	10:28.0	-19:56:04	G10.6-0.4	4.84	-3				1	-0.22	0.05	6.00E-04	high	3	1234		14	
289	10:46.9	-17:34:15	G012.72+0.69	1.24	17.3	1.60E+22			1	-0.35	0.04		2		3			
290	10:50.6	-17:55:46	G012.418+0.506	1.24	18.3	1.40E+23	1.60E+04	8.10E+02	1,7	-0.71	1.64	7.20E-03	high	3	13		12	
291	11:31.3	-19:30:41	G011.109-0.397	4.85	0.3	8.90E+22	3.50E+03	6.30E+03	1,7	-0.71	1.93	2.00E-02	high	3	3		12	
292	11:32.0	-19:30:39	G11.11-0.4	4.85	1				1				high	3	3		14,18	
293	11:51.1	-17:31:30	G12.89+0.49	1.25					2	-0.45			high		1234	19		
294	11:58.6	-19:36:04	G011.082-0.534	2.85	29.5	9.10E+22	3.20E+04	1.90E+03	1	-0.32	0.79	7.70E-03	high	2	1		12	
295	12:11.2	-18:41:35	G011.902-0.141	3.83	37.9	8.90E+22	7.20E+03	2.40E+03	1,7	-0.53	1.74	1.20E-02	high	3	234		12	
296	13:56.3	-17:28:36	G013.169+0.077	3.86	49.7	3.10E+22	3.80E+04	6.30E+02	1	-0.62	1.45	7.20E-03	high	2			12	
297	14:01.3	-17:28:39	G013.178+0.059	3.86	49.4	9.10E+22	6.10E+03	2.40E+03	1	-0.43	1.36	8.90E-03	high	2	123		12	
298	14:08.2	-17:57:04	G012.77-0.19	2.95	35.6	1.40E+23			1	-0.61			2		3			
299	14:10.0	-17:27:22	G013.213+0.039	3.87	51.9	5.80E+22	3.00E+03	5.10E+03	1	-0.29	0.64	5.50E-03	high	3			12	
300	14:12.6	-17:57:34	G012.776-0.211	2.95	35.5	3.50E+22	1.30E+04	7.40E+02	1	-0.39	0.66	2.50E-03	high	1			12	
301	14:22.1	-17:52:02	G012.87-0.20	2.95	35.5	1.00E+23			9	-0.12	0.36		2		3			
302	14:36.8	-17:29:25	G013.234-0.071	3.85	38.1	3.00E+22	7.70E+04	7.10E+02	1	-0.73	1.31	8.90E-03	high	2			12	
303	14:39.6	-17:48:36	G012.96-0.23	2.94	35.2	1.20E+23			1	-0.62	2.02		2	3	3			
304	14:41.2	-17:29:23	G013.243-0.086	2.95	36.8	1.40E+23	1.90E+04	2.20E+03	1	-0.33	0.89	8.00E-03	high	2	13		12	
305	14:41.8	-17:54:23	G012.878-0.287	2.93	33.4	5.40E+22	7.30E+04	8.30E+01	1,7	-0.5	1.28	2.00E-03	high	3			12	
306	14:42.3	-17:37:10	G013.131-0.152	3.85	45.1	5.50E+22	9.10E+03	1.30E+03	1,7	-0.64	1.01	4.90E-03	high	3	1		12	

Table A.1
(Continued)

No.	R.A.	Decl.	Alias	Dist.	V_{LSR}	$N(\text{H}_2)$	$n(\text{H}_2)$	Mass	Lines	δv	V_{in}	\dot{M}_{in}	Type	Stage	Maser	Outflow	Reference
307	15:37.3	+03:48:19	LDN 492	0.24	7.7	3.90E+21	6.50E+04		2,11	-0.35	0.04	4.40E-06	low	1			6,24,31
308	15:37.7	-17:34:06	G013.281-0.321	3.85	41	3.50E+22	2.40E+05	4.70E+02	1,7	-1.16	2.13	1.60E-02	high	2			12
309	15:39.9	-17:34:37	G013.28-0.34-MM1	3.85	41.3	2.90E+22			1,4	-0.59	1.09	1.50E-03	high				13
310	15:40.0	-17:34:44	G013.276-0.334	3.85	41.3	5.20E+22	5.60E+03	2.80E+03	1,7	-1	1.32	9.20E-03	high	1			12
311	15:41.0	-17:33:18	G013.299-0.326	3.85	40.5	2.50E+22	2.50E+04	5.20E+02	1,7	-0.83	1.45	5.60E-03	high	1			12
312	16:22.0	-16:53:02	G013.97-0.15	3.85	40.2	4.50E+22			1,9	-0.53	0.09			2			3
313	16:38.2	-16:51:09	G014.02-0.19	3.85	40	7.00E+22			1,9	-0.47	0.45			2			3
314	16:40.7	-16:45:48	G014.11-0.16	3.86	39.1	2.80E+22			1	-0.48	0.34			2			3
315	16:59.4	-18:02:30	LDN 328-IRS	1.25	6.7				9	-0.66	0.04	7.20E-07	low	2			26
316	17:01.3	-16:38:48	G014.25-0.17	3.86	38.3	7.10E+22			1	-0.78			high	2			3
317	17:02.3	-16:38:21	G014.26-0.17	3.86	38.5	6.40E+22			1,9	-0.85	0.44			2			3
318	17:16.5	-17:01:16	G013.97-0.45-MM1	3.06	20				1	-0.73	0.31		high				13
319	17:34.8	-17:06:52	G013.91-0.51-MM1	3.02	23	7.70E+22			1,3	-0.64	0.69	2.20E-03	high				13
320	17:35.1	-17:06:53	G013.902-0.516	3.01	23.3	4.80E+22	1.40E+04	7.80E+02	1,7	-1.59	1	4.00E-03	high	2			12
321	18:12.7	-16:49:34	G014.227-0.511	1.84	19.4	1.60E+23	1.20E+04	1.50E+03	1,7	-0.51	1.16	7.00E-03	high	2	123		12
322	18:13.1	-16:57:20	G014.114-00.574	3.06	20.1	1.30E+03	8.00E+02		1,7	-0.52	2	3.80E-03	high	2	13		28
323	18:57.2	-13:40:14	G017.09+0.82	1.87	22.4	3.90E+22			1,9	-0.85	0.04			2			3
324	19:02.9	-16:30:29	G014.63-0.57-MM3	1.83	17.4	5.20E+22			4				high				13
325	19:11.2	-16:29:56	G014.626-0.562	1.83	18	2.80E+22	1.90E+03	5.40E+02	1,7	-0.66	1.25	2.10E-03	high	1	123		12
326	19:12.1	-13:33:32	G017.19+0.81-MM3	1.87	22.7	5.30E+22			1,4	-0.35	1.65	2.80E-03	high	3			13
327	19:12.5	-16:19:49	G014.777-0.487	3.08	21.8	2.30E+22	4.90E+03	5.00E+03	1	-0.46	0.52	5.20E-03	high	2			12
328	19:12.9	-13:33:46	G017.19+0.81-MM2	1.88	22.8	1.70E+23			1	-0.48	0.66	3.10E-03	high	3			13
329	19:14.3	-16:30:41	G014.63-0.57-MM2	1.84	18.4	1.50E+23			3,4	-0.78			high		123		13
330	19:15.2	-16:29:59	G014.63-0.57-MM1	1.84	18.6	2.60E+23			3,4,5	-2.06	2.7	2.20E-02	high		123		13
331	19:17.4	-16:44:04	G014.39-0.75A-MM2	1.83	17.6				1,4	-0.45			high				13
332	19:19.0	-16:43:49	G014.39-0.75A-MM1	1.83	17.8	5.70E+22			1,4	-0.52			high				13
333	19:33.3	-16:45:01	G014.39-0.75B-MM3	4.88		5.70E+22			1	-5.79			high				13
334	20:24.8	-16:11:35	M17S	1.85	20		5.00E+05		1		1.4	4.00E-04	high	3	1234		14,15
335	20:50.8	-14:06:01	G016.93+0.24-MM1	1.5	23.8	4.20E+22			1	-0.62			high				13
336	21:09.1	-14:31:49	IRAS18182-1433	3.84	59.1				1,3,12	-0.44			high	2	1234	Y	27
337	21:09.2	-14:31:47	IRAS18182-1433	3.84	59		1.40E+04	1.30E+03	6	-0.35	1.99	1.10E-02	high	3	1234	Y	1
338	21:10.0	-14:31:44	IRAS18182-1433	3.84	59				1		1.74	1.60E-02	high	2	1234	Y	14,17
339	25:01.8	-13:09:06	G018.26-0.24-MM5	3.93	66.6	6.00E+22			4				high				13
340	25:04.5	-13:08:27	G018.26-0.24-MM4	3.95	68.8	5.70E+22			5	-1.14			high		1234		13
341	25:05.6	-13:08:20	G018.26-0.24-MM3	3.94	68.6	7.10E+22			1,4,5	-1.12	6.1	1.60E-02	high		1234		13
342	25:06.4	-13:08:51	G018.26-0.24-MM2	3.94	67.8	8.90E+22			1,4,5	-1.03			high		1234		13
343	25:10.7	-12:42:28	IRAS18223-1243	3.24	45.5				1	-0.31			high	2			27

Table A.1
(Continued)

No.	R.A.	Decl.	Alias	Dist.	V_{LSR}	$N(\text{H}_2)$	$n(\text{H}_2)$	Mass	Lines	δv	V_{in}	\dot{M}_{in}	Type	Stage	Maser	Outflow	Reference
344	25:11.8	-13:08:04	G018.26-00.24-MM1	3.94	68.4	9.80E+22			1,4,5	-1.18			high	13		13	
345	25:54.4	-11:52:34	G019.472+0.171	1.5	19.5	1.40E+23	1.30E+03	2.80E+04	1	-0.51	2.58	5.20E-02	high	2	1234		12
346	27:38.3	-11:56:40	G19.61-0.23	3.27	43	1.00E+23	4.60E+06	1.50E+01	1,13,15	-0.37	0.21	1.40E-03	high	3	1234		10,14,16,20
347	28:10.7	-11:28:48	G20.08-0.14	4.06	42				1		0.05	3.00E-04	high	3	1234		14,15,16
†348	29:47.5	+01:17:01	Serp S68N	0.24	8.8				12	-1.61			low	2	14	Y	22
†349	29:51.2	+01:16:41	Serp SMM 5	0.24	8.4				11,12	-0.74			low	2	14	Y	22
†350	29:56.7	+01:13:16	Serp SMM 4	0.24	8.1				2,3,11,12	-0.4			low	2	13	Y	22
351	30:00.2	+01:02:12	G031.41+5.24	0.24	8.3	9.70E+21			1	-1.22							3
352	30:02.3	-12:15:38	IRAS18272-1217	3.29	34				1	-1.2			high	2			27
†353	30:14.4	-01:33:33	J1830144-013333	0.24	8.1				9	-0.24	0.17	8.10E-06	low	2			26
†354	30:15.6	-02:07:19	J1830156-020719	0.24	6.7				9	-0.9	0.27	5.50E-05	low	2			26
†355	30:16.2	-01:52:52	J1830162-015252	0.24	6.7				9	-0.83	0.22	2.00E-05	low	2			26
356	31:35.4	-01:54:21	G028.97+3.54	0.24	7.2	1.40E+22			1,9	-1.29	0.44			2			3
357	31:43.3	-09:22:28	IRAS18290-0924	4.74	84.3				2,3	-0.34			high	2	1234		27
358	32:14.5	-01:59:24	G028.97+3.36	0.24	7.3	2.50E+22			1,9	-1.25				2			3
†359	32:17.2	-01:59:11	G028.97+3.35	0.24	7.3	2.30E+22			1	-2.8				2			3
†360	32:42.4	-02:47:56	J1832424-024756	0.24	6.3				9	-0.47	0.1	4.30E-06	low	2			26
361	33:15.2	-00:46:22	G030.17+3.69	0.24	9.1	6.40E+21			1,9	-0.46							3
362	34:23.5	-08:32:20	G023.28-00.12-MM1	5.3	99	6.50E+22			1	-0.47			high	3			13
363	36:18.3	-07:41:00	G024.37-00.15-MM2	3.65	56.2	4.40E+22			1,5	-1.11			high				13
364	36:27.8	-07:40:24	G024.37-00.15-MM1	3.6	59.2	4.90E+22			1,4	-0.59			high	1			13
365	36:27.9	-07:40:25	IRAS18337-0743	3.64	57.9				1	-0.52			high	2	1		27
366	37:12.2	-07:11:23	G024.94-00.15-MM2	3.79	48.2	5.50E+22			1,4	-0.66	3	6.20E-03	high	2	3		13
367	37:19.7	-07:11:41	G024.94-00.15-MM1	3.79	47.4	6.50E+22			1,3,4,5	-0.8	1.34	3.30E-03	high	3			13
368	37:21.3	-07:33:07	G024.61-00.33-MM2	3.77	43.6	3.50E+22			4	-0.07			high				13
369	37:23.1	-07:31:39	G024.61-00.33-MM1	3.77	42.8	5.90E+22			1,4,5	-0.72			high	24			13
†370*	38:08.1	-06:46:52	G025.382-00.147	5.77	96.7		2.00E+06	4.70E+01	10		1.3	2.00E-03	high	2	134		11
†371*	38:40.3	-05:35:06	IRAS18360-0537	6.06	103.5		8.00E+06	1.00E+01	13		1.5	1.50E-03	high	2	134		8
372	39:04.7	-06:24:21	G025.82-0.18	5.47	93.7	5.60E+22			1	-0.37	1.53		high	2	1234		3
373	39:36.8	-05:54:42	G026.32-0.07	5.87	100.3	2.70E+22			1,9	-0.5	1.21			2			3
374	39:55.9	-05:38:52	IRAS18372-0541	1.75	23.6				1	-0.59			high	2	23		27
375	43:01.8	-04:14:27	G028.20-0.07	5.68	97.1	5.10E+22			1	-0.26	0.06		high	2	13	Y	3
376	45:12.2	-02:01:12	IRAS18426-0204	1.78	15				12	-0.41			high	2	23		27
377	46:22.4	-02:14:20	IRAS18437-0216	7.15	110.8				1,3,12	-0.4			high	2	3		27
378	47:33.0	-01:12:36	G31.41+0.31	5.17	97				1	-0.65			high	3	1234		14,15
379	47:34.4	-01:12:46	G31.41+0.31	14.33					2	-0.65			high	3	1234		19
380	47:36.8	-03:15:15	G029.60-0.63	4.27	77.2	3.60E+22			1	-0.98	1.77	8.90E-03	high	2	23		3
381	47:41.9	-01:52:13	G030.90	5.42	92.8				1,4	-0.42	1.76	9.40E-03	high				13
			+00.00B-MM2														
382	47:48.2	-01:51:30	G030.90	5.47	94.3	4.30E+22			1,4	-0.27			high				13
			+00.00C-MM3														

Table A.1
(Continued)

No.	R.A.	Decl.	Alias	Dist.	V_{LSR}	$N(\text{H}_2)$	$n(\text{H}_2)$	Mass	Lines	δv	V_{in}	\dot{M}_{in}	Type	Stage	Maser	Outflow	Reference	
383	48:39.7	-03:03:56	IRAS18460-0307	4.38	83.7				1,12	-0.64			high	2			27	
384	49:52.2	-00:18:57	IRAS18472-0022	2.51	49				1,12	-0.57			high	2			27	
385	52:20.3	+00:26:20	G033.42+0.00	2.02	10.6	4.00E+21			1	-1.02				2	23		3	
386	53:16.7	+01:14:43	G034.25+0.16	5.17	58.1	1.90E+23			1,9	-3.55				2	1234		3	
388	53:18.4	+01:15:00	IRAS18507	3.33	57.8				1,2,10	-0.27			high	3	1234		19,20	
			+0110															
387	53:18.4	+01:14:57	W44	3.33	58.5				7.60E+04	1.60E+03	6	-0.66	4.83	5.30E-02	high	3	1234	1
389	53:18.5	+01:14:58	G34.26+0.15	5.17	58				3.60E+05		1		1.5	1.40E-03	high	3	1234	Y
†390	53:18.6	+01:14:58	G34.26+0.15	13.99					1.10E+08	76(11)	1,10,13		1	1.00E-04	high	3	1234	Y
391	53:23.2	+01:53:16	G034.85	3.21	55.7					4				high			13	
			+00.43-MM1															
392	54:40.6	+01:38:04	IRAS18521	5.07	76				1,2,12	-0.89			high	2	12		27	
			+0134															
393	56:58.2	+01:18:44	G034.71-00.63-MM2	2.51	45.8	5.20E+22			1,3	-0.35			high				13	
394	57:05.2	+02:06:29	G035.49-0.30A-MM1	3.99	55.6	6.60E+22			1,4	-0.66	7.4	1.70E-02	high		3		13	
395	57:08.1	+02:10:47	G035.49-0.30B-MM3	2.5	45.9	4.20E+22			4	-0.18			high				13	
396	57:08.4	+02:09:01	G035.49-0.30B-MM2	2.5	45.4	5.30E+22			4	-0.2	0.84	1.40E-03	high				13	
397	57:40.7	+01:16:09	G034.77-0.81-MM1	2.48	43.7				1,4	-0.76			high				13	
398	57:53.3	+04:18:17	IRAS18553	0.92	10				1,2,12	-0.57			high	2	134		27	
			+0414															
399	59:04.7	+03:38:57	G037.05-0.03	4.58	81.3	3.30E+22			1	-0.29				2	234		3	
400	01:54.0	+04:12:49	G037.87-00.40	4.2	58.8				1				high	3	34		14,18	
401	01:55.3	+02:07:55	G036.02-1.36	2.18	31.8	8.60E+21			1,9	-0.6	0.26						3	
402	03:44.7	+05:33:45	G039.28-0.19	4.06	70.5	2.20E+22			9	-0.34				2			3	
403	03:45.1	+05:40:45	IRAS19012	3.7	65.8				2,3,12	-0.65			high	2	1234	Y	27	
			+0536															
404	07:32.0	+05:15:46	G039.45-1.17	0.36	12.7	3.80E+21			1	-0.36	0.06			2			3	
405	10:34.0	+09:08:24	G043.24-00.05	0.29	7.3				1		1.27	5.60E-02	high	3	13		14,18	
406	19:48.4	+14:02:27	IRAS19175	0.79	14.6				3	-0.32			high	2	3		27	
			+1357															
407	22:42.6	+14:09:44	G049.07-0.33	5.13	60.4	3.00E+22			1	-0.54			high	2	13		3	
408	24:19.7	+14:38:03	IRAS19220	5.35	68.8				1,2,3,12	-0.4			high	2	2		27	
			+1432															
409	26:52.8	+13:49:35	G049.25-1.38	0.06	5.7	5.90E+21			9	-1.64							3	
410	29:04.2	+17:55:16	G053.10+0.11	1.31	22.2	8.90E+21			9	-0.21	0.09			2			3	
411	29:08.9	+17:55:14	G053.11+0.09	1.31	22	1.10E+22			1	-0.3	0.19			2			3	
412	29:12.7	+17:55:52	G053.12+0.08	1.31	22.3	2.40E+22			1,9	-0.58	0.12			2			3	
413	29:12.9	+17:56:59	G053.14+0.09	1.32	22.3	1.50E+22			1,9	-0.83	0.03			2			3	
414	30:19.6	+17:44:19	G053.08-0.24	1.43	23.6	6.50E+21			1	-0.99				2			3	
415	30:55.7	+18:29:55	G053.81-00.00-MM1	1.56	24.1	6.90E+22			1,4	-0.34	7.4	9.60E-03	high				13	
†416	37:01.4	+07:34:07	B335 SMM1	0.3	8.4				2,11,12	-0.46			low	2		Y	22	
†417	41:04.5	+10:57:02	LDN 694-2	0.4	9.6	4.60E+21	1.80E+04		2,11	-0.46	0.05	4.90E-06	low	1			6,24,31	
418	43:11.0	+23:44:06	IRAS19410	2.16	22.4				1,3,12	-0.64			high	2	1234	Y	27	
			+2336															
419	43:29.0	+23:40:22	IRAS19413	2.16	20.8				1,3,12	-0.48			high	2	3		27	
			+2332															
420	46:20.0	+24:35:29	G060.88-00.13	2.17	23.3				1				high	3	13	Y	14,18	

Table A.1
(Continued)

No.	R.A.	Decl.	Alias	Dist.	V_{LSR}	$N(\text{H}_2)$	$n(\text{H}_2)$	Mass	Lines	δv	V_{in}	M_{in}	Type	Stage	Maser	Outflow	Reference
†421	10:13.1	+27:28:17	IRAS20081 +2720	0.09	5.7				1	-0.93			high	2	3		27
422	19:39.0	+40:56:38	G78.438+2.659	2.17	3.3				1				high	3	3		14,18
423	27:25.7	+37:22:52	SH 2-106 FIR	3.41	-1				1	-0.34			high	3	34		20
†424	31:15.2	+40:22:21	G079.24+0.53	2.59	0.3	2.60E+22			1	-0.4	0.71			2			3
425	34:19.9	+40:31:12	G079.71+0.15	2.53	1	4.90E+21			1,9	-0.57	0.12			2			3
426	34:58.8	+41:34:47	IRAS20332 +4124	2.65	-2				1,12	-0.41			high	2			27
427	35:51.9	+43:02:36	G081.90+1.43	2	11	4.80E+21			1,9	-1.77	0.02						3
428	35:56.7	+42:48:48	G081.72+1.28	2.19	3.7	1.10E+22			1,9	-0.72	0.16						3
429	39:00.7	+42:23:07	G081.72+0.57	2.29	-3.1	1.40E+23			1	-0.69	0.97	3.40E-02		2	1234	Y	3
430	39:00.9	+42:22:50	W75OH	2.29	-3.3				1,2,10,11	-0.39			high		1234	Y	19,20
431	39:01.0	+42:19:53	G081.68+00.54	1.55	-8.2				1		0.26	3.60E-04	high	3	123	Y	14,18
432	39:06.5	+68:02:13	LDN 1157	0.87	2.7				2,11,12	-0.33			low	2	13	Y	22
433	40:56.6	+67:23:04	LDN 1148B	0.87	2.6				9	-1.14	0.11	2.30E-06	low	2			26
434	42:39.2	+42:25:23	G082.17+0.07	1.67	10.1	1.00E+22			1,9	-0.29	0.01			2			3
435	42:58.8	+67:48:18	LDN 1155C-2	0.87	1.6	1.90E+21	6.60E+03		11	-0.47	0.07	3.90E-06	low	1			6,24
†436	43:30.0	+67:52:42	LDN 1155C-1	0.87	2.9	2.10E+21	5.10E+04		11	-0.48	0.09	2.30E-05	low	1			6,24
437	49:27.8	+41:25:54	G082.18-1.54	1.56	2.8	8.40E+21			9	-0.12							3
438	49:30.8	+41:27:23	G082.21-1.53	1.56	2.7	1.00E+22			9	-0.21		2.00E-04		2			3
439	58:15.6	+43:48:54	G085.05-1.25	5.12	-37.5	1.10E+22			1,9	-0.82	0.41			2		Y	3
†440	00:13.2	+50:20:50	LDN 981-1	1.61	0	1.20E+21	5.00E+03		11	-0.39	0.1	1.10E-05	low	1			6,24
441	02:21.2	+67:54:20	IRAS 21017+6742	0.87	2.9				9	-0.62	0.22	1.70E-05	low	2		Y	26
442	02:27.3	+67:54:18	J21022744 +6754186	0.87	2.8				9	-0.63	0.16	1.00E-05	low	2		Y	26
443	44:57.0	+47:41:52	J21445706 +4741529	0.67	1.6				9	-0.58	0.16	1.20E-05	low	2		Y	26
444	15:09.0	+58:49:09	IRAS22134 +5834	2.81	18.5				1				high	2	3	Y	14,17
†445	28:33.3	+62:58:29	G107.50+4.47	0.78	-2.1	2.50E+22			1,9	-0.47		1.00E-04		2		Y	3
446	29:59.4	+75:14:03	IRAS 22290+7458	0.77	-4				9	-0.84	0.24	1.10E-05	low	2			26
†447	37:02.3	+58:57:21	LDN 1197	0.77	-3.1	2.00E+21	2.70E+04		11	-0.41	0.05	2.20E-06	low	1			6,24
448	38:47.1	+75:11:29	LDN 1251B	0.77	1				11,12	-0.73			low	2	3	Y	22
449	47:13.0	+62:11:41	G108.99+2.73	0.8	-10.5	2.60E+22			1,9	-0.44	0.16			2			3
†450	56:17.9	+62:01:49	Cep A	0.79	-10	1.00E+06			1,10	-0.59	0.23	1.70E-05	high	3	1234	Y	14,15,20
451	58:15.9	+62:35:29	G110.32+2.52	0.79	-12.1	1.40E+22			1,9	-0.73	0.08						3
452	01:58.6	+61:50:44	G110.40+1.67	0.79	-11.2	5.80E+21			1	-1.56							3
†453	03:13.1	+61:42:26	IRAS23011 +6126	0.79	-11				2	-0.41			low	2	13	Y	25
454	13:44.9	+61:26:51	NGC7538	2.69	-56				1,11	-0.34			high	3	1234	Y	20,21
455	17:21.0	+59:28:49	IRAS23151 +5912	2.7	-56				1				high	2	13	Y	14,17
†456	25:46.5	+74:17:38	CB 244	0.7	3.8				2	-1.02			low	2		Y	25

Appendix All Collected Infall Sources

Table A.1 is the complete version of table 3. See section 2.2 for details of each column.

ORCID iDs

- Shuling Yu (于书岭) <https://orcid.org/0000-0002-8617-3521>
- Zhibo Jiang (江治波) <https://orcid.org/0000-0002-5920-031X>
- Yang Yang (杨旸) <https://orcid.org/0000-0002-2895-7707>
- Zhiwei Chen (陈志维) <https://orcid.org/0000-0003-0849-0692>
- Haoran Feng (冯浩然) <https://orcid.org/0000-0003-1714-0600>

References

- Beltrán, M. T., & de Wit, W. J. 2016, *A&AR*, **24**, 6
- Beuther, H., Sridharan, T. K., & Saito, M. 2005, *ApJL*, **634**, L185
- Bonnell, I. A., & Bate, M. R. 2002, *MNRAS*, **336**, 659
- Bonnell, I. A., Vine, S. G., & Bate, M. R. 2004, *MNRAS*, **349**, 735
- Cesaroni, R., Galli, D., Lodato, G., Walmsley, C. M., & Zhang, Q. 2007, in Protostars and Planets V, ed. B. Reipurth, D. Jewitt, & K. Keil (Tucson, AZ: Univ. Arizona Press), 197
- Churchwell, E., Sievers, A., & Thum, C. 2010, *A&A*, **513**, A9
- Contreras, Y., Sanhueza, P., Jackson, J. M., et al. 2018, *ApJ*, **861**, 14
- Cunningham, N., Lumsden, S. L., Moore, T. J., Maud, L. T., & Mendigutía, I. 2018, *MNRAS*, **477**, 2455
- De Vries, C. H., & Myers, P. C. 2005, *ApJ*, **620**, 800
- Di Francesco, J., Myers, P. C., Wilner, D. J., Ohashi, N., & Mardones, D. 2001, *ApJ*, **562**, 770
- Djordjevic, J. O., Thompson, M. A., Urquhart, J. S., & Forbrich, J. 2019, *MNRAS*, **487**, 1057
- Evans, N. J. 1999, *ARA&A*, **37**, 311
- Faúndez, S., Bronfman, L., Garay, G., et al. 2004, *A&A*, **426**, 97
- Fuller, G. A., Williams, S. J., & Sridharan, T. K. 2005, *A&A*, **442**, 949
- Gregersen, E. M. 1998, Collapse and Beyond: an Investigation of the Star Formation Process, PhD Thesis, The Univ. of Texas at Austin
- Gregersen, E. M. 2000, *ApJ*, **533**, 440
- Gregersen, E. M., Evans, N. J., II, Zhou, S., & Choi, M. 1997, *ApJ*, **484**, 256
- Guzmán, A. E., Sanhueza, P., Contreras, Y., et al. 2015, *ApJ*, **815**, 130
- He, Y. X., Zhou, J. J., Esimbek, J., et al. 2015, *MNRAS*, **450**, 1926
- He, Y. X., Zhou, J. J., Esimbek, J., et al. 2016, *MNRAS*, **461**, 2288
- Hogerheijde, M. R., & Van Der Tak, F. F. 2000, *A&A*, **362**, 697
- Keown, J., Schnee, S., Bourke, T. L., et al. 2016, *ApJ*, **833**, 97
- Keto, E., Caselli, P., & Rawlings, J. 2015, *MNRAS*, **446**, 3731
- Kim, M.-R., Lee, C. W., Maheswar, G., Myers, P. C., & Kim, G. 2021, *ApJ*, **910**, 112
- Klaassen, P. D., Testi, L., & Beuther, H. 2012, *A&A*, **538**, A140
- Klaassen, P. D., & Wilson, C. D. 2007, *ApJ*, **663**, 1092
- Klaassen, P. D., & Wilson, C. D. 2008, *ApJ*, **684**, 1273
- Klassen, M., Pudritz, R. E., Kuiper, R., Peters, T., & Banerjee, R. 2016, *ApJ*, **823**, 28
- Kurtz, S., Churchwell, E., & Wood, D. O. S. 1994, *ApJS*, **91**, 659
- Lee, C. W., & Myers, P. C. 2011, *ApJ*, **734**, 60
- Lee, C. W., Myers, P. C., & Tafalla, M. 1999, *ApJ*, **526**, 788
- Lee, C. W., Myers, P. C., & Tafalla, M. 2001, *ApJS*, **136**, 703
- Leung, C. M., & Brown, R. L. 1977, *ApJL*, **214**, L73
- Li, Y., Xu, Y., Sun, Y., et al. 2019, *ApJS*, **242**, 19
- Li, Z. Y., Banerjee, R., Pudritz, R. E., et al. 2014, in Protostars and Planets VI, ed. H. Beuther, R. S. Klessen, C. P. Dullemond, & T. Henning (Tucson, AZ: Univ. Arizona Press), 173
- Liu, S.-Y., Su, Y.-N., Zinchenko, I., et al. 2020, *ApJ*, **904**, 181
- Liu, T., Wu, Y., & Zhang, H. 2013, *ApJ*, **776**, 29
- Liu, T., Wu, Y., Zhang, Q., et al. 2011, *ApJ*, **728**, 91
- Mardones, D., Myers, P. C., Tafalla, M., et al. 1997, *ApJ*, **489**, 719
- Maud, L. T., Moore, T. J., Lumsden, S. L., et al. 2015, *MNRAS*, **453**, 645
- McKee, C. F., & Tan, J. C. 2002, *Nature*, **416**, 59
- McKee, C. F., & Tan, J. C. 2003, *ApJ*, **585**, 850
- Motte, F., Bontemps, S., & Louvet, F. 2018, *ARA&A*, **56**, 41
- Myers, P. C., Mardones, D., Tafalla, M., Williams, J. P., & Wilner, D. J. 1996, *ApJL*, **465**, L133
- Padoa, P., Haugbolle, T., & Nordlund, Å. 2014, *ApJ*, **797**, 32
- Peretto, N., Fuller, G. A., Duarte-Cabral, A., et al. 2013, *A&A*, **555**, A112
- Qin, S. L., Schilke, P., Wu, J., et al. 2016, *MNRAS*, **456**, 2681
- Qiu, K., Zhang, Q., Beuther, H., & Fallscheer, C. 2012, *ApJ*, **756**, 170
- Redman, M. P., Khanzadyan, T., Loughnane, R. M., & Carolan, P. B. 2008, in ASP Conf. Ser. 387, Massive Star Formation: Observations Confront Theory, ed. H. Beuther, H. Linz, & T. Henning (San Francisco, CA: ASP), 38
- Reid, M. J., Dame, T. M., Menten, K. M., & Brunthaler, A. 2016, *ApJ*, **823**, 77
- Reid, M. J., Menten, K. M., Brunthaler, A., et al. 2019, *ApJ*, **885**, 131
- Reiter, M., Shirley, Y. L., Wu, J., et al. 2011, *ApJ*, **740**, 1
- Rygl, K. L. J., Wyrowski, F., Schuller, F., & Menten, K. M. 2013, *A&A*, **549**, A5
- Saral, G., Audard, M., & Wang, Y. 2018, *A&A*, **620**, A158
- Sarrasin, E., Abdallah, D. B., Wernli, M., et al. 2010, *MNRAS*, **404**, 518
- Schnee, S., Brunetti, N., Di Francesco, J., et al. 2013, *ApJ*, **777**, 121
- Schöier, F. L., Van Der Tak, F. F., Van Dishoeck, E. F., & Black, J. H. 2005, *A&A*, **432**, 369
- Shirley, Y. L., Evans, N. J., II, Young, K. E., Knez, C., & Jaffe, D. T. 2003, *ApJS*, **149**, 375
- Shu, F. 1987, *ARA&A*, **25**, 23
- Smith, R. J., Shetty, R., Beuther, H., Klessen, R. S., & Bonnell, I. A. 2013, *ApJ*, **771**, 24
- Sohn, J., Lee, C. W., Park, Y., et al. 2007, *ApJ*, **664**, 928
- Sridharan, T. K., Beuther, H., Schilke, P., Menten, K. M., & Wyrowski, F. 2002, *ApJ*, **566**, 931
- Storm, S., Mundy, L. G., Lee, K. I., et al. 2016, *ApJ*, **830**, 127
- Su, Y.-N., Liu, S.-Y., Li, Z.-Y., et al. 2019, *ApJ*, **885**, 98
- Su, Y., Yang, J., Yan, Q.-Z., et al. 2021, *ApJ*, **910**, 131
- Sun, Y., & Gao, Y. 2009, *MNRAS*, **392**, 170
- Tan, J. C., Beltrán, M. T., Caselli, P., et al. 2014, in Protostars and Planets VI, ed. H. Beuther, R. S. Klessen, C. P. Dullemond, & T. Henning (Tucson, AZ: Univ. Arizona Press), 149
- Tang, M. Y., Qin, S. L., Liu, T., & Wu, Y. F. 2019, *RAA*, **19**, 040
- Tsamis, Y. G., Rawlings, J. M., Yates, J. A., & Viti, S. 2008, *MNRAS*, **388**, 898
- Vasyunina, T., Linz, H., Henning, T., et al. 2011, *A&A*, **527**, A88
- Wang, K., Zhang, Q., Testi, L., et al. 2014, *MNRAS*, **439**, 3275
- Wu, J., & Evans, N. J., II. 2003, *ApJL*, **592**, L79
- Wu, Y., Qin, S. L., Guan, X., et al. 2009, *ApJ*, **697**, 116
- Wu, Y., Wei, Y., Zhao, M., et al. 2004, *A&A*, **426**, 503
- Wu, Y., Zhu, M., Wei, Y., et al. 2005, *ApJL*, **628**, L57
- Xu, Y., Reid, M., Dame, T., et al. 2016, *SciA*, **2**, e1600878
- Yang, Y., Jiang, Z.-B., Chen, Z.-W., et al. 2020a, *RAA*, **20**, 115
- Yang, Y. L., Evans, N. J., Smith, A., et al. 2020b, *ApJ*, **891**, 61
- Yorke, H. W., & Sonnhalter, C. 2002, *ApJ*, **569**, 846
- Yuan, J., Li, J.-Z., Wu, Y., et al. 2018, *ApJ*, **852**, 12
- Yue, Y. H., Qin, S. L., Liu, T., et al. 2021, *RAA*, **21**, 14
- Zhang, G. Y., Xu, J. L., Vasyunin, A. I., et al. 2018, *A&A*, **620**, A163
- Zhang, Q., Sridharan, T. K., Hunter, T. R., et al. 2007, *A&A*, **470**, 269
- Zhang, S., Yang, J., Xu, Y., et al. 2020, *ApJS*, **248**, 15
- Zhou, S. 1992, *ApJ*, **394**, 204
- Zhou, S., Evans, N. J. I., Koempe, C., & Walmsley, C. M. 1994, *ApJ*, **421**, 854
- Zhou, S., Evans, N. J. I., Koempe, C., & Walmsley, C. M. 1993, *ApJ*, **404**, 232
- Zinnecker, H., & Yorke, H. W. 2007, *ARA&A*, **45**, 481